

Machine learning tagged boosted dark photon: A signature of fermionic portal matter at the LHC

Shivam Verma ^{*a}, Sanjoy Biswas ^{†a}, Tanumoy Mandal ^{‡b}, and Subhadip Mitra ^{§c,d}

^a*Department of Physics, Ramakrishna Mission Vivekananda Educational and Research Institute, Belur Math, Howrah 711202, India*

^b*Department of Physics, Indian Institute of Science Education and Research Thiruvananthapuram, Vithura, Kerala, 695551, India*

^c*Center for Computational Natural Science and Bioinformatics, International Institute of Information Technology, Hyderabad 500 032, India*

^d*Center for Quantum Science and Technology, International Institute of Information Technology, Hyderabad 500 032, India*

Abstract

We use machine learning techniques to identify a boosted dark photon jet as a signature of a heavy vector-like fermionic portal matter (PM) connecting the visible and the dark sectors. In this work, the fermionic PM which mixes only with the standard model (SM) third generation up-type quark, dominantly decays to a top quark and dark photon pair. The dark photon then *promptly* decays to a pair of standard model fermions via the gauge kinetic mixing. We have analyzed two different final states, namely, (i) exactly one tagged dark photon and exactly one tagged top quark jet, and (ii) at least two tagged dark photons and at least one tagged top quark jet at the 13 and 14 TeV LHC center of mass energies. Both these final states receive significant contributions from the pair and single production processes of the top partner. The rich event topology of the signal processes, *i.e.*, the presence of a boosted dark photon and top quark jet pair, along with the fact that the invariant mass of the system corresponds to the mass of the top partner, help us to significantly suppress the potential SM backgrounds. We have shown that one can set a 2σ exclusion limit of 2.6 TeV on the top partner mass with $\sin\theta_L = 0.1$ and assuming 100% branching ratio of the top partner in the exactly one tagged dark photon and exactly one tagged top quark jet final state at the 14 TeV LHC center of mass energy assuming 300 fb^{-1} of integrated luminosity.

*shivam.59910103@gm.rkmvu.ac.in

†sanjoy.phy@gm.rkmvu.ac.in

‡tanumoy@iisertvm.ac.in

§subhadip.mitra@iiit.ac.in

1 Introduction

Extending the Standard Model (SM) of particle physics with an additional dark sector (DS) gives a theoretically well-motivated framework to explain the existence of dark matter (DM) and associated phenomenologies. So far, various theoretical models within this framework have been proposed in the literature. Many of these scenarios consider the DS interacting with the SM sector via portal interactions [1–4]. A gauge kinetic mixing portal is one such example for the DS-SM interaction. The simplest way to realize it would be to assume that the dark sector contains an abelian dark $U(1)_d$ gauge group under which all the SM particles are neutral. The corresponding gauge boson, i.e., the dark photon, becomes massive via the (dark) Higgs mechanism.

Any ultraviolet completion of such a model will introduce additional particle-like states, known as the portal matter, which are charged under both the SM and the $U(1)_d$ gauge groups. These states can be either scalars or fermions. Here, we consider an additional vector-like fermion, specifically a vector-like quark (VLQ), as a portal matter that produces the gauge kinetic mixing via loop contribution. The VLQ can also mix with the SM fermions depending on its charge assignment. We assume the VLQ to be a singlet under the $SU(2)_L$ interaction and carry $+2/3$ unit of $U(1)_Y$ charge. As it also has a non-zero $U(1)_d$ charge, a Yukawa-type interaction involving the VLQ, a SM up-type quark, and the Higgs is not allowed. However, a similar Yukawa-type interaction term can be introduced with a charged dark Higgs, which can generate the mixing between SM fermions and the vector-like quark as it acquires a non-zero vacuum expectation value (VEV). To avoid the current constraints on the VLQ mixing with the first two generations of quarks, we assume the VLQ mixes only with the third-generation quark with the same electric charge, i.e., the top quark. (In a broader setup, a VLQ that transforms non-trivially under $SU(2)_L$ is another possibility, but it is beyond the scope of the present article.) Earlier, Refs. [5, 6] showed that, in such a setup, the VLQ could predominantly decay to a top quark and a dark photon or a dark Higgs, while its traditional decay modes, such as $T_p \rightarrow bW$, tZ , and th , became suppressed. The origin of the large branching ratio into these non-standard modes can be traced to the hierarchies between (i) the SM top quark and VLQ mass, (ii) the VEVs of the two Higgs fields, and (iii) the mixing angle of the SM top quark with the VLQ and their mass ratio [5, 6]. Other non-standard decay modes of VLQs have attracted significant attention in the current literature [7–31].

VLQs as portal matters have been getting due attention—there are dedicated studies on their searches in collider experiments [1, 2, 4, 6, 13, 18, 25, 32–34]. The main focus of the current study is to analyze the LHC signatures of such a vector-like quark in the mass range of 1.2 TeV to 3.0 TeV, decaying into a highly boosted dark photon and a top quark pair. In this scenario, the dark photon decays into SM fermions via gauge kinetic mixing, controlled by the corresponding gauge kinetic mixing parameter, ε . Depending on the dark photon mass, this parameter is strongly constrained by various experiments, including low-energy ones [35, 36]. For the mass range 1 – 10 GeV (relevant for our LHC analysis), the bound on the kinetic mixing parameter is $\varepsilon \lesssim 10^{-3}$. However, a very small ε could result in the dark photon decaying outside the detector. We fix this parameter by requiring the dark photon to decay promptly to SM final states ($\gamma_d \rightarrow f\bar{f}$, $f = \text{leptons, quarks}$) inside the detector. Nevertheless, a long-lived dark photon decaying inside the detector presents an interesting possibility, which will be explored in future work.

Searching for dark photon signals at collider experiments is an ongoing quest. In this article, we propose, a machine learning (ML) based method to identify a highly boosted dark photon in its hadronic decay mode, which can carry the imprint of a heavy VLQ acting as a portal matter at collider experiments. Machine learning techniques have been used widely in the field of particle physics, in particular, in the context of jet physics [37–44]. To identify dark photon jets we employ an algorithm based on a Hybrid Deep Neural Network (HDNN) framework. This approach combines a Convolutional Neural Network (CNN) and a Multi-Layer Perceptron (MLP) [45–47]. The CNN models jet images, and the MLP captures the jet-level features of both signal (initiated by dark photons) and background (initiated by other particles) jets. We focus on a light dark photon of mass around 10 GeV, which is more likely to be mimicked by background jets, making the jet invariant mass a poor discriminator. We show how machine learning techniques can significantly improve the tagging efficiency of such

low-mass dark photons.

We emphasize that one of our objective is to provide a method for identifying a boosted dark-photon jet among various other jets present in an event. This task essentially involves the *binary classification* between a dark photon jet and other non-dark photon jets, such as those initiated by quarks, gluons, τ leptons, or top quarks, across a wide range of transverse momenta. Moreover, even though we consider dark photon production in the decay of a heavy VLQ that mixes only with the up-type third-generation quark in this paper, our analysis of dark photon tagging is more general and applicable to VLQs mixing with other generations as well. The tagging algorithm functions effectively across a wide range of VLQ masses, with only a moderate change in the tagging efficiency. The technique employed in this work can be used whenever the decay of a heavy particle produces a highly boosted “light exotic particle” (such as the dark photon).

The present work focuses on two different final states: *(i)* exactly one tagged dark photon and exactly one tagged top quark jet (ED1ET1), and *(ii)* at least two tagged dark photons and at least one tagged top quark jet (AD2AT1) in the context of the 13 and 14 TeV LHC center-of-mass energies. Most studies in the literature focus on single and pair production separately by choosing different final states. However, disentangling these two processes is generally challenging. As we will demonstrate, the final states we consider—mainly to characterize the single and pair productions of the top partner—exhibit a significant admixture of both processes. Moreover, the relative admixture of these two processes in a given final state strongly depends on the mixing angle between the top and top partner. Thus, it becomes crucial to analyze different final states rather than individual single and pair production processes. We have proposed a set of kinematic observables by utilizing the topology of signal events to suppress the SM background in the above-mentioned final states. We propose a set of kinematic observables to suppress the SM background for these final states and optimize the signal significance. In addition, we also consider the current LHC limits on the model and constrain the relevant parameter space.

The rest of the paper is organized as follows. In Section 2, we briefly describe the theoretical framework we have considered. Section 3 consists of collider analysis of the signal and background processes. Results and discussions are presented in Section 4. Finally, we conclude in Section 5.

2 Theoretical framework

In this section, we will briefly summarize the theoretical framework detailed in [5, 6]. We have considered an extension of the SM with a VLQ transforming under the $SU(2)_L$ gauge group as a singlet while being charged under both the $U(1)_Y$ and an additional $U(1)_d$ gauge groups with corresponding charges, $+2/3$ and $+1$, respectively. The gauge boson corresponding to the $U(1)_d$ gauge group is referred as “dark photon” and the SM particles are neutral under this gauge group.

The model also contains a complex scalar field Φ_d that is singlet under the SM gauge group and charged under $U(1)_d$. The charge assignment of the relevant fields under $SU(3)_C \times SU(2)_L \times U(1)_Y \times U(1)_d$ gauge group are presented in Table 1. The complex scalar field Φ_d is accountable for the mixing of the VLQ with SM fermions having same charges and generating the mass for the dark photon via the higgs mechanism in the dark sector. In this work we have considered VLQ mixing with only the top quark to avoid flavor constraints.

Fields	$SU(3)_C$	$SU(2)_L$	Y	Y_d
t'_R	3	1	2/3	0
b_R	3	1	-1/3	0
$Q_L = \begin{pmatrix} t'_L \\ b_L \end{pmatrix}$	3	2	1/6	0
Φ	1	2	1/2	0
T'_L	3	1	2/3	1
T'_R	3	1	2/3	1
Φ_d	1	1	0	1

Table 1: Representations of the relevant fields under the full symmetry group of the theory. Here, t' is the third generation up-type quark of the SM in interaction basis and T' is the vector-like top partner also in the interaction basis.

Below we describe three relevant sectors corresponding to the above-mentioned model, namely, the (i) gauge ($\mathcal{L}_{\text{Gauge}}$), (ii) scalar ($\mathcal{L}_{\text{Scalar}}$), and (iii) fermion ($\mathcal{L}_{\text{Fermion}}$) sectors.

- Gauge sector:

$$\mathcal{L}_{\text{Gauge}} = -\frac{1}{4}G_{\mu\nu}^a G^{a,\mu\nu} - \frac{1}{4}W_{\mu\nu}^i W^{i,\mu\nu} - \frac{1}{4}B'_{\mu\nu} B'^{\mu\nu} + \frac{\varepsilon'}{2 \cos \theta_W} B'_{d,\mu\nu} B'^{\mu\nu} - \frac{1}{4}B'_{d,\mu\nu} B_d'^{\mu\nu}, \quad (1)$$

where $G_{\mu\nu}^a$ are the $SU(3)_C$ field strength tensor with $a = 1, \dots, 8$; $W_{\mu\nu}^i$ are $SU(2)_L$ field strength tensor with $i = 1, 2, 3$; $B'_{\mu\nu}$ is that of the $U(1)_Y$ and $B'_{d,\mu\nu}$ corresponds the field strength tensor of the additional $U(1)_d$ group. The kinetic mixing term between the $U(1)_Y$ and $U(1)_d$ field strength tensors is parameterized by ε' .

- Scalar sector:

$$\mathcal{L}_{\text{Scalar}} = |D_\mu \Phi|^2 + |D_\mu \Phi_d|^2 - V(\Phi, \Phi_d) \quad (2)$$

Here, Φ represents the SM Higgs field, while Φ_d denotes the corresponding Higgs field in the dark sector. The gauge covariant derivative in general has the form:

$$D_\mu = \partial_\mu - ig_S t^a G_\mu^a - ig T^i W_\mu^i - ig' Y B'_\mu - ig'_d Y_d B'_{d,\mu} \quad (3)$$

In this expression, g_S , g , g' , and g'_d are the coupling constants corresponding to the $SU(3)_C$, $SU(2)_L$, $U(1)_Y$, and $U(1)_d$ gauge groups, respectively. Here, t^a and T^i are the generators of the $SU(3)_C$ and $SU(2)_L$ groups, respectively in appropriate representation. Also, Y and Y_d corresponds to the $U(1)_Y$ and $U(1)_d$ charges, respectively.

The scalar potential takes the form:

$$V(\Phi, \Phi_d) = -\mu^2 |\Phi|^2 + \lambda |\Phi|^4 - \mu_{h_d}^2 |\Phi_d|^2 + \lambda_{h_d} |\Phi_d|^4 + \lambda_{hh_d} |\Phi|^2 |\Phi_d|^2 \quad (4)$$

The fluctuation of the two scalar fields around the classical minima can be parameterized as:

$$\Phi = \begin{pmatrix} 0 \\ \frac{v_{\text{EW}} + h'}{\sqrt{2}} \end{pmatrix}, \quad \Phi_d = \frac{1}{\sqrt{2}}(v_d + h'_d) \quad (5)$$

Where v_{EW} is fixed at 246 GeV, by the masses of the electroweak gauge bosons while v_d can be fixed by the dark gauge coupling (g_d) and the mass of the dark photon. However, we will work with v_d and m_{γ_d} as free parameters.

As a consequence of this, $SU(3)_C \times SU(2)_L \times U(1)_Y \times U(1)_d$ is reduced to $SU(3)_C \times U(1)_{\text{EM}}$ and the gauge bosons corresponding to the broken generators becomes massive.

To scalar mass matrix can be diagonalized using the orthogonal transformation described below,

$$\begin{pmatrix} h \\ h_d \end{pmatrix} = \begin{pmatrix} \cos \theta_S & -\sin \theta_S \\ \sin \theta_S & \cos \theta_S \end{pmatrix} \begin{pmatrix} h' \\ h'_d \end{pmatrix} \quad (6)$$

In the mass eigenbasis, h corresponds to the observed Higgs with mass $m_h = 125$ GeV, while h_d denotes the dark Higgs field with mass m_{h_d} . The free parameters of the scalar sector are the scalar mixing angle θ_S , m_{h_d} , and v_d .

- Fermion sector: The lagrangian for the fermion sector focusing solely on the 3rd generation quarks and VLQ is given by,

$$\mathcal{L}_{\text{Fermion}} = \bar{Q}_L i \not{D} Q_L + \bar{t}'_R i \not{D} t'_R + \bar{b}_R i \not{D} b_R + \bar{T}' i \not{D} T' + \mathcal{L}_{\text{Yuk}} \quad (7)$$

where \mathcal{L}_{Yuk} is given by,

$$\mathcal{L}_{\text{Yuk}} = -y_b \bar{Q}_L \Phi b_R - y_t \bar{Q}_L \tilde{\Phi} t'_R - \lambda_T \Phi_d \bar{T}'_L t'_R - m_T \bar{T}'_L T'_R + h.c.. \quad (8)$$

When Φ and Φ_d get VEVs, the mass matrix in t' and T' basis takes the form,

$$\mathcal{L}_{u3\text{-mass}} = -\bar{\chi}_L \mathcal{M} \chi_R + h.c., \quad (9)$$

where

$$\chi_\tau = \begin{pmatrix} t'_\tau \\ T'_\tau \end{pmatrix}, \quad \mathcal{M} = \begin{pmatrix} \frac{y_t v_{\text{EW}}}{\sqrt{2}} & 0 \\ \frac{\lambda_T v_d}{\sqrt{2}} & m_T \end{pmatrix}, \quad (10)$$

and $\tau = L, R$.

One requires a bi-unitary transformation of the following kind in order to diagonalize the above mass matrix

$$\begin{pmatrix} t_L \\ T_{pL} \end{pmatrix} = \begin{pmatrix} \cos \theta_L & -\sin \theta_L \\ \sin \theta_L & \cos \theta_L \end{pmatrix} \begin{pmatrix} t'_L \\ T'_L \end{pmatrix}, \quad \begin{pmatrix} t_R \\ T_{pR} \end{pmatrix} = \begin{pmatrix} \cos \theta_R & -\sin \theta_R \\ \sin \theta_R & \cos \theta_R \end{pmatrix} \begin{pmatrix} t'_R \\ T'_R \end{pmatrix} \quad (11)$$

The lighter mass eigenstate (t) appearing in above equation will be identified as the observed top quark having mass, $m_t = 173.5$ GeV and T_p denotes the heavier mass eigenstate, to be referred as the top partner. Mass of the top partner (m_{T_p}) and the mixing angle involving the left chiral top and top partner fields (θ_L) are the two free parameters of the fermion sector. The parameters appearing in the lagrangian of the fermion sector can be written in terms of these free parameters as,

$$\lambda_T = \frac{(m_{T_p}^2 - m_t^2) \sin 2\theta_L}{\sqrt{2} v_d \sqrt{m_t^2 \cos^2 \theta_L + m_{T_p}^2 \sin^2 \theta_L}} \quad (12)$$

$$m_T = \frac{m_t m_{T_p}}{\sqrt{m_t^2 \cos^2 \theta_L + m_{T_p}^2 \sin^2 \theta_L}} \quad (13)$$

In the context of the present work, the relevant independent free parameters of the model described above are m_{T_p} , $\sin \theta_L$, m_{γ_d} , v_d , m_{h_d} , $\sin \theta_S$. The gauge kinetic mixing parameter (ε) is also a free parameter¹ of this model, however, we set it to a fixed value consistent with the observations.

¹ ε is related to ε' via $\varepsilon = \varepsilon' / \sqrt{1 - \varepsilon'^2 / \cos^2 \hat{\theta}_W}$, where $\cos \hat{\theta}_W = \cos \theta_W + \mathcal{O}(\varepsilon^2)$

2.1 Constraints

Even though the model parameters are considered free some of them are subjected to constraints coming from observations and theoretical consistency. Below we present three such important constraints on the parameters that represent a portal interaction between the SM and the dark sector.

- Gauge sector (ε): The kinetic mixing parameter is strongly constrained by various low-energy observations in the case of a massive dark photon scenario. These constraints on ε depend significantly on the mass of the dark photon [35, 36]. For dark photons with mass $m_{\gamma_d} \gtrsim$ a few GeVs, the allowed range of ε is $\lesssim 10^{-3}$. However, since we will be interested in the case where the dark photon decays inside the detector, we restrict working with arbitrarily small value of ε consistent as it plays a crucial role in the context of dark photon tagging. For example, if the $\varepsilon \sim 10^{-7}$, the decay of dark photon will decay with a displaced vertex that can be utilized as an additional feature to enhance its tagging efficiency. However, in the present work, we only consider the prompt decay of the dark photon by fixing the value of ε at 10^{-4} . Any other value in the range $10^{-3} - 10^{-6}$ is acceptable as long as it meets the above requirements. We leave the long-lived dark photon scenario for future work.
- Scalar sector ($\sin \theta_S$): The mixing angle between the SM Higgs and the dark Higgs is constrained by various observations such as, direct searches at the LEP experiment, LHC heavy Higgs searches, the Higgs signal strength measurement, correction to the W boson mass, perturbative unitarity and LHC higgs invisible searches. [48–53]. However, these constraints depend on the mass of the dark higgs and the dark higgs VEV (v_d). For dark higgs in the mass range ($10 \text{ GeV} \leq m_{h_d} < 100 \text{ GeV}$) and $v_d \sim v_{EW}$ the LEP experiment provides a stringent lower limit of $0.9 - 0.998$ on the allowed values of $|\sin \theta_S|$. In the range $100 \text{ GeV} \leq m_{h_d} \leq 400 \text{ GeV}$, the strongest limit on $|\sin \theta_S| < 0.2$ comes from the LHC heavy Higgs searches [51, 53]. For higher masses, the stringent limit comes from the correction to the W boson mass. In fact, $|\sin \theta_S| \gtrsim 0.14$ can be ruled out for $m_{h_d} \sim 1 \text{ TeV}$ [53]. The mixing angle is also constrained by the higgs invisible searches in the case when $h \rightarrow \gamma_d \gamma_d$ is allowed. The CMS [54] and ATLAS [55] limits on this invisible branching ratio set a strong constraint on the mixing angle as a function of the dark higgs VEV:

$$|\sin \theta_S| \leq 4.6 \times 10^{-4} \left(\frac{v_d}{\text{GeV}} \right) \sqrt{\text{BR}_{\text{lim}}} \quad (14)$$

where BR_{lim} is 0.15 (CMS) and 0.107 (ATLAS). For $v_d = 100 \text{ GeV}$, this translates to $|\sin \theta_S| \leq 0.018$ (CMS) and 0.015 (ATLAS). Throughout our analyses we set, $|\sin \theta_S| = 10^{-4}$.

- Fermion sector (λ_T): The perturbative unitarity requirement coming from the process $h_d t \rightarrow h_d t$ process controlled by the parameter λ_T gives an upper bound on it, $\lambda_T < 4\sqrt{2\pi}$. On the other hand the reality condition on the top and top partner mixing angle ($\sin \theta_L$) also gives an independent constraint on λ_T .

The mixing angle can be written as,

$$|\sin \theta_L| = \frac{1}{2} \left[\frac{2m_{T_p}^2 - 2m_t^2 - \lambda_T^2 v_d^2}{m_{T_p}^2 - m_t^2} \left(1 - \sqrt{1 - \frac{8\lambda_T^2 v_d^2 m_t^2}{(2m_{T_p}^2 - 2m_t^2 - \lambda_T^2 v_d^2)^2}} \right) \right]^{1/2} \quad (15)$$

The reality requirement implies $|\lambda_T| < \sqrt{2}(m_{T_p} - m_t)/v_d$ [5, 6] The combination of both of these can together be given as,

$$|\lambda_T| < \sqrt{2} \min \left(\frac{m_{T_p} - m_t}{v_d}, 4\sqrt{\pi} \right) \quad (16)$$

2.2 T_p decay width

In this model, the top partner decays to both in the standard ($T_p \rightarrow bW, tZ, th$) and non-standard ($T_p \rightarrow t\gamma_d, th_d$) modes. Below we present the partial decay widths of the top partner in various decay modes in the limit $|\sin \theta_d|, |\sin \theta_s|, \varepsilon, m_t/m_{T_p} \ll 1$ [6, 56, 57]:

- $T_p \rightarrow bW$:

$$\Gamma(T_p \rightarrow bW) \approx \frac{1}{16\pi} \frac{m_{T_p}^3}{v_{EW}^2} \sin^2 \theta_L \quad (17)$$

- $T_p \rightarrow tV (V = Z, \gamma_d)$:

$$\Gamma(T_p \rightarrow tZ) \approx \frac{1}{32\pi} \frac{m_{T_p}^3}{v_{EW}^2} \sin^2 \theta_L \cos^2 \theta_L \quad (18)$$

and

$$\Gamma(T_p \rightarrow t\gamma_d) \approx \frac{1}{32\pi} \frac{m_{T_p}^3}{v_d^2} \sin^2 \theta_L \cos^2 \theta_L \times \left(1 + \frac{m_{T_p}^2 m_t^2}{D^2} \right) \quad (19)$$

- $T_p \rightarrow tS (S = h, h_d)$:

$$\Gamma(T_p \rightarrow th) \approx \frac{1}{32\pi} \frac{m_{T_p}^3}{v_{EW}^2} \sin^2 \theta_L \cos^2 \theta_L \quad (20)$$

and,

$$\begin{aligned} \Gamma(T_p \rightarrow th_d) \approx & \frac{1}{32\pi} \frac{m_{T_p}^3}{v_d^2} \sin^2 \theta_L \cos^2 \theta_L \\ & \times \frac{m_{T_p}^4}{D^2} \left(\sin^4 \theta_L + \frac{m_t^2}{m_{T_p}^2} \cos^4 \theta_L + 4 \frac{m_t^2}{m_{T_p}^2} \sin^2 \theta_L \cos^2 \theta_L \right) \end{aligned} \quad (21)$$

where, $D = m_t^2 \cos^2 \theta_L + m_{T_p}^2 \sin^2 \theta_L$.

We use the following values for the relevant SM parameters to calculate the top partner decay branching ratios and the cross-section in the later part of our analysis [58],

$$\begin{aligned} m_h &= 125.5 \text{ GeV}, \quad m_t = 173.2 \text{ GeV}, \quad m_b = 4.18 \text{ GeV} \\ m_W &= 80.377 \text{ GeV}, \quad m_Z = 91.187 \text{ GeV}, \quad v_{EW} = 246 \text{ GeV} \end{aligned}$$

In Fig. 1, we depict the branching ratio of the top partner in various modes as a function of $\sin \theta_L$ for various choices of $v_d, m_{\gamma_d}, m_{h_d}$, and m_{T_p}

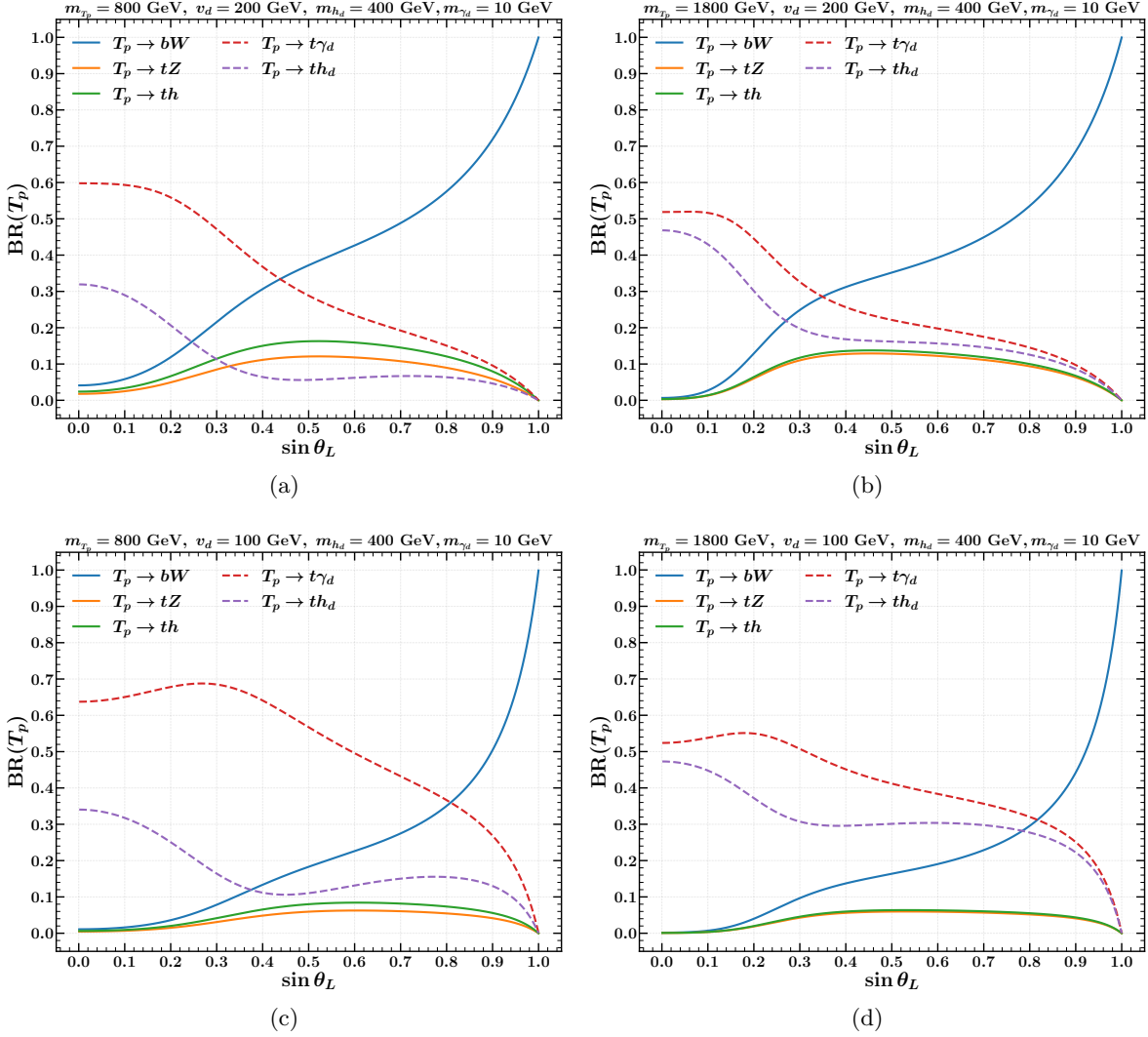


Figure 1: Top partner branching ratio in the standard (solid line) and non-standard modes (dashed line) as a function of the mixing angle between top and top partner ($\sin \theta_L$) for different bench mark points, (a) $m_{T_p} = 800 \text{ GeV}$ and (b) $m_{T_p} = 1.8 \text{ TeV}$ with $v_d = 200 \text{ GeV}$ and $m_{h_d} = 400 \text{ GeV}$. The same for (c) $m_{T_p} = 800 \text{ GeV}$ and (d) $m_{T_p} = 1.8 \text{ TeV}$ with $v_d = 100 \text{ GeV}$ and $m_{h_d} = 200 \text{ GeV}$. The dark photon mass is assumed to be 10 GeV for all the four plots.

3 Collider analysis

In this section, we detail the collider analysis of signal and background processes. We have considered both the single ($pp \rightarrow T_p j$) and the pair ($pp \rightarrow T_p \bar{T}_p$) production of the vector like top partner. We have used MadGraph5_aMC@NLO (version 3.2.0) [59] event generator to simulate both the single and pair production processes of top partner at 13 and 14 TeV LHC energies. In order to achieve this, we have implemented the model described in Sec. 2 at the Lagrangian level with the help of FeynRules [60]. The Universal FeynRules Output [61] is then interfaced with MadGraph5_aMC@NLO for event generation. We have used NNPDF (version 2.3) [62] parton distribution functions to simulate the parton-parton hard scattering in a pp collision. Events generated by MadGraph are then interfaced with PYTHIA (version 8.307) [63] for parton shower, hadronization, and further analysis. The energy and momenta of all the final state objects are smeared with appropriate Gaussian smearing function to take into account the finite detector resolution effects. The details of smearing function parameterization can be found in [6].

In this work, we are considering the top partner decaying to a top quark and dark photon. The dark photon further decays to SM fermions via the gauge kinetic mixing parameter. Since the top

partner is expected to be heavy ($\gtrsim 1$ TeV) in order to satisfy the current LHC bounds, the top and the dark photon produced in the decay of it are highly boosted. *One of our primary objectives in this study is to investigate the hadronic decays of the dark photon and the top quark, along with their subsequent identification and reconstruction.*

We use a HDNN framework that uses a combination of convolutional neural network and multi layer perceptron to identify and reconstruct a dark photon jet while a jet initiated by a top quark is reconstructed using John-Hopkins top tagger [64]. To ensure the hadronic decays of the top quark and the dark photon we have vetoed events with isolated leptons. We first proceed for identification and reconstruction of jets coming from the light exotic particle i.e. (in this analysis which corresponds to a dark photon). In order to achieve this we cluster all the final state hadrons to construct jets of radius 0.4 using anti- k_T jet clustering algorithm (AK4). We have used FastJet (v3.4.0) [65] to cluster the hadrons.

Out of all the jets thus formed we select only jets with $p_T > 200$ GeV as potential dark photon jet candidates and prepare jet images and other high level features for machine learning based identification. We have utilized two different images of a single high p_T jet of clustering radius 0.4 in the $\eta - \phi$ plane and a subjet inside it of radius 0.2 around the jet center, with corresponding granularities 0.1 and 0.025, respectively. In addition, a set of crucial jet level features, such as, p_T , p_T fraction, charge multiplicity and charge multiplicity fraction of the potential dark photon jet candidates help us in identifying a dark photon initiated jet very effectively. It is possible to achieve an average tagging efficiency of 66% to 88% for the dark photon jet in the top partner mass range, 1.2 – 1.8 TeV. The average mistagging rate for the corresponding non-dark photon jets present in the signal and in the SM background varies in the range 1.0% to 1.5%. The details of the ML based identification and reconstruction of the dark photon are described in Appendix A. We only analyze an event further if it contains at least one identified dark photon jet.

The remaining part of the event analysis proceeds in the following manner depending on the number of identified dark photon jets:

1. If the number of ML tagged dark photon jet is *one* we remove² all of its constituents and re-cluster the remaining hadrons of that event with a total E_T dependent clustering radius R using Cambridge-Aachen (C-A) clustering algorithm [66]. The re-clustering is done only if the total E_T of the remaining hadrons is more than 400 GeV. These jets are then analyzed using John-Hopkins top tagger to identify a boosted top quark structure in it. We keep the event if a top quark initiated jet is obtained. A subset of this event category will give rise to a final state comprising *exactly one* dark photon jet and *exactly one* top quark jet which dominantly consists of contribution coming from the single production of top partner and only a fraction of events coming from pair production of top partner.
2. If the number of dark photon jets is *more than one* then we remove the constituents of the identified dark photon jets in a pair wise manner. For example, if the number of dark photon jets is *two* then we remove the constituents of both, the leading and the sub-leading dark photon jets simultaneously, if it is *three* then we have three possible pairs. We consider each possible pair one at a time and remove all the constituents of that pair. The remaining hadrons in all the cases are then re-clustered as prescribed before with a total E_T dependent clustering radius R to find a top structure in the jets thus formed using John-Hopkins top tagger. This has been done keeping in mind the topology of events where the top partner is pair produced and further decays to a top quark and a dark photon giving rise to *exactly two* dark photon jets in the final state. We keep an event only if *at least one* top quark jet is identified in these events. Therefore, this category contains events mostly coming from pair production of top partner with a small fraction of events coming from single production of top partner.

The John-Hopkins top tagger mentioned above, iteratively de-clusters a C-A clustered jet to find the substructure inside a fat jet of radius R . The J-H top tagging algorithm requires the specification

²We identify and remove the constituents of the dark photon jets before the top reconstruction to make sure same total E_T dependent clustering radius, as used in our previous analysis [6], where the dark photon was treated as an invisible particle.

of the following additional parameters: the fraction of the jet p_T carried by a subjet and the Manhattan distance (defined as $|\Delta\eta|+|\Delta\phi|$) between two subjets to satisfy minimum values, δ_p and δ_r , respectively to be considered as hard and resolved. We tabulate, in Table 2, the values of R , δ_p and δ_r for different total transverse momentum of an event [6].

E_T	400	600	800	1000	1600	2600
R	1.4	1.2	1.0	0.8	0.6	0.4
δ_p	0.10	0.10	0.05	0.05	0.05	0.05
δ_r	0.19	0.19	0.19	0.19	0.19	0.19

Table 2: Choices of jet clustering radius(R), minimum jet p_T fraction carried by the subjet (δ_p), minimum manhattan distance between two subjets (δ_r) for various range of total transverse momentum in an event excluding the contribution of dark photon transverse momentum.

In Table 3, we summarize the effect of basic cut, *i.e.* requiring *at least two* central jets (defined with $p_T > 20$ GeV and $|\eta| < 2.5$), no isolated leptons and $H_T > 500$ GeV, followed by requirement of tagging *at least one* dark photon jet out of jets having $p_T > 200$ GeV and *at least one* tagged top quark in an event for the signal process.

\sqrt{s} (TeV)	Process	m_{T_p} (TeV)	Production cross-section (fb)	Basic cut (fb)	$p_T \geq 200$ GeV (fb)	γ_d tagging (fb)	Top tagging (fb)
13	$T_p\bar{T}_p$	1.2	11.40	8.33	8.32	6.84	1.86
		1.4	3.42	2.58	2.58	2.25	0.66
		1.6	1.11	0.86	0.86	0.78	0.24
		1.8	0.38	0.30	0.30	0.28	0.09
		2.0	0.13	0.11	0.11	0.10	0.03
	$T_p j$	1.2	20.92	17.18	16.42	10.69	2.81
		1.4	12.16	10.13	9.82	7.33	2.02
		1.6	7.33	6.24	6.08	4.90	1.31
		1.8	4.50	3.90	3.82	3.22	0.84
		2.0	2.82	2.49	2.45	2.13	0.53
14	$T_p\bar{T}_p$	1.2	16.15	11.90	11.90	9.77	2.61
		1.4	5.06	3.82	3.82	3.32	0.97
		1.6	1.72	1.34	1.34	1.21	0.37
		1.8	0.61	0.49	0.49	0.45	0.14
		2.0	0.23	0.18	0.18	0.17	0.05
	$T_p j$	1.2	26.65	21.86	20.86	13.55	3.50
		1.4	15.81	13.21	12.76	9.47	2.58
		1.6	9.70	8.26	8.06	6.48	1.72
		1.8	6.09	5.27	5.18	4.35	1.09
		2.0	3.91	3.45	3.40	2.95	0.74

Table 3: The effects of cut flow on cross-sections for the single and pair production of the top partner at both $\sqrt{s} = 13$ and 14 TeV LHC center of mass energies. $\sin\theta_L = 0.1$ is assumed to estimate the cross-section for the various benchmark points assuming $\text{BR}(T_p \rightarrow t\gamma_d) = 100\%$ and $\text{BR}(\gamma_d \rightarrow q\bar{q}) = 100\%$. In addition, $v_d = 200$ GeV, $m_{\gamma_d} = 10$ GeV and $m_{h_d} = 400$ GeV are used to obtain the above results.

We have analyzed two different final states, namely,

- **ED1ET1:** *exactly one* dark photon jet + *exactly one* top quark jet ($\gamma_d + t$) and,
- **AD2AT1:** *at least two* dark photon jets + *at least one* top quark jet ($\geq 2\gamma_d + \geq t$).

This categorization of final states have been done keeping in mind the event topology of the single and pair production of the top partner. The schematic diagram illustrating the topology of the final

states is depicted in Fig. 2. However, given the finite tagging efficiencies for both the top quark and the dark photon the two final states are populated by events coming from both single and pair production of top partner. While the AD2AT1 mostly characterizes the pair production of top partner process (99% to 90% for m_{T_p} in the range 1.2 TeV to 2 TeV), the ED1ET1 consists of a substantial admixture of both single (74% to 98% for m_{T_p} in the range 1.2 TeV to 2 TeV) and pair (26% to 0.02% in the range 1.2 TeV to 2 TeV) production of the top partner.

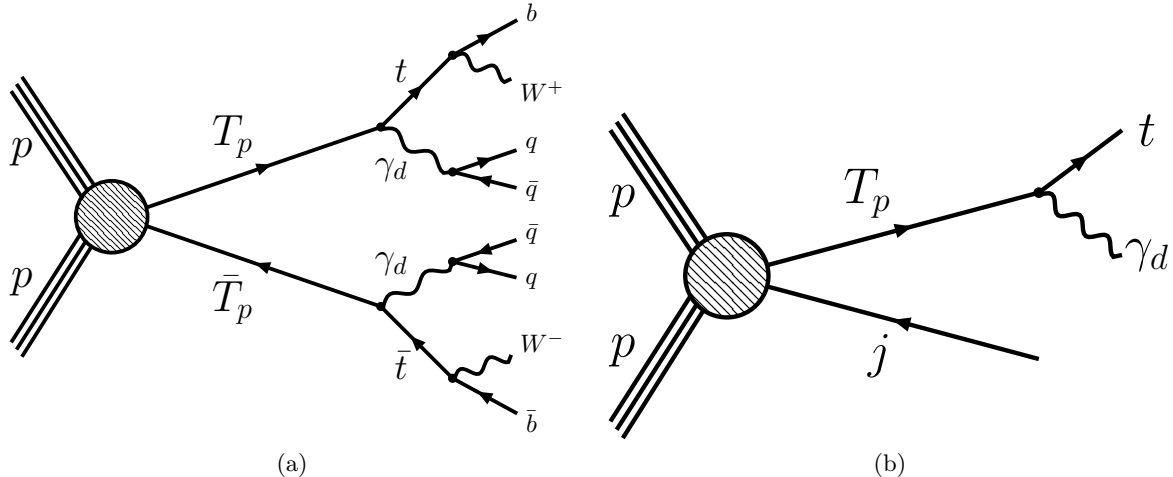


Figure 2: Schematic diagrams of signal processes: (a) $pp \rightarrow T_p \bar{T}_p$ and (b) $pp \rightarrow T_p j$ with subsequent decays of $T_p \rightarrow t \gamma_d$ and $\gamma_d \rightarrow q \bar{q}$.

The relevant standard model backgrounds for both the final states are $t\bar{t} + jets$, $t\bar{t}W$, $t\bar{t}Z$ and QCD multi-jet process which might give rise to one or more top quark jets and jets mistagged as dark photon. Given the rich topology of the signal events, only the first three give the dominant contributions and are considered in this analysis. In Table 4, the effect of basic cut followed by the requirement of tagging *at least one* dark photon jet out of jets having $p_T > 200$ GeV and *at least one* tagged top quark in an event for the SM background processes are summarized. The $t\bar{t} + jets$ background has been generated with the highest jet multiplicity two at the matrix element level and implemented MLM [67] jet parton matching algorithm to avoid double counting. In this analysis the $t\bar{t} + jets$ is considered at aN³LO and $t\bar{t}Z$, $t\bar{t}W$ are considered at NLO+NNLL in QCD by multiplying the leading order cross-sections obtained from MadGraph with appropriate k -factors [6].

\sqrt{s} (TeV)	Process	Production cross-section (fb)	Basic cut (fb)	$p_T \geq 200$ GeV (fb)	γ_d tagging (fb)	Top tagging (fb)
13	$t\bar{t} + jets$	41728.84	41600.84	28009.07	507.79	91.18
	$t\bar{t}Z$	863.00	490.29	138.75	3.11	0.46
	$t\bar{t}W$	566.00	273.52	64.43	1.67	0.30
14	$t\bar{t} + jets$	51297.49	51142.23	34490.00	621.15	107.31
	$t\bar{t}W$	653.00	320.24	76.65	1.96	0.35
	$t\bar{t}Z$	1045.00	600.27	173.52	3.99	0.56

Table 4: The effects of cut flow on cross-sections for the SM background processes relevant for our analysis at both $\sqrt{s} = 13$ and 14 TeV LHC center of mass energies.

One can see from Table 4 that the requirement of boosted dark photon jet in the SM background event gives a suppression factor of more than 1 in 100 (can also be seen in App. A). In addition, requirement of the presence of at least one boosted top quark jet in the final state reduces the SM background by a factor of 4 to 7 depending on the particular SM background process.

3.1 Kinematic variables

For both the final state considered in this analysis the following set of kinematical variables are found to be useful to separate the signal from the background events.

Transverse momentum of tagged dark photon

In Fig. 3 and Fig. 4 we plot the transverse momentum, defined as $p_T = \sqrt{p_x^2 + p_y^2}$, of the ML identified dark photon jet for two different final states considered in this analysis at $\sqrt{s} = 13$ and 14 TeV, respectively.

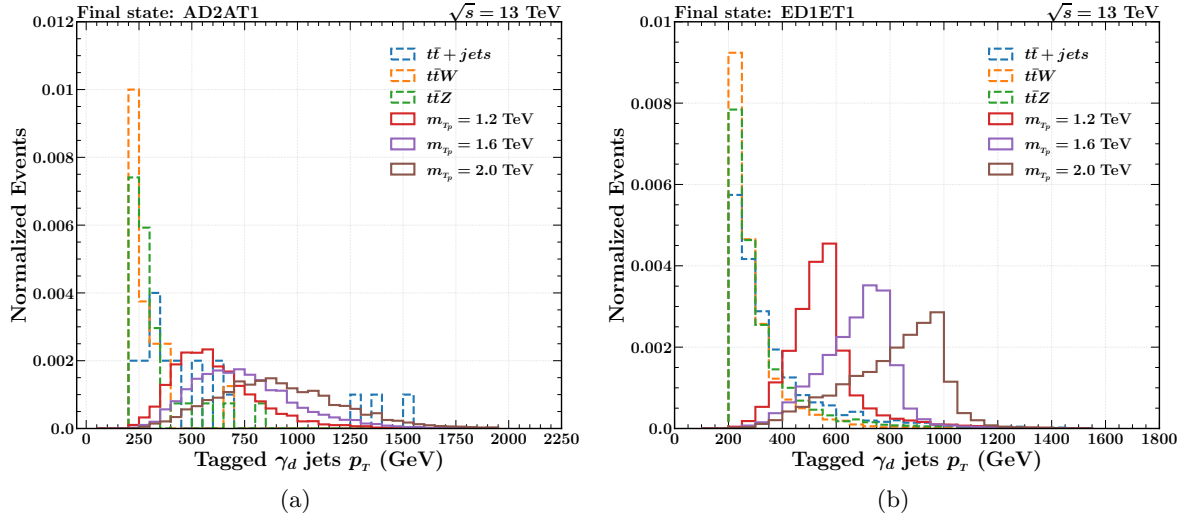


Figure 3: Transverse momentum distributions of the ML identified dark photon jet for signal and backgrounds in the (a)AD2AT1 and (b)ED1ET1 final states at 13 TeV LHC center of mass energy.

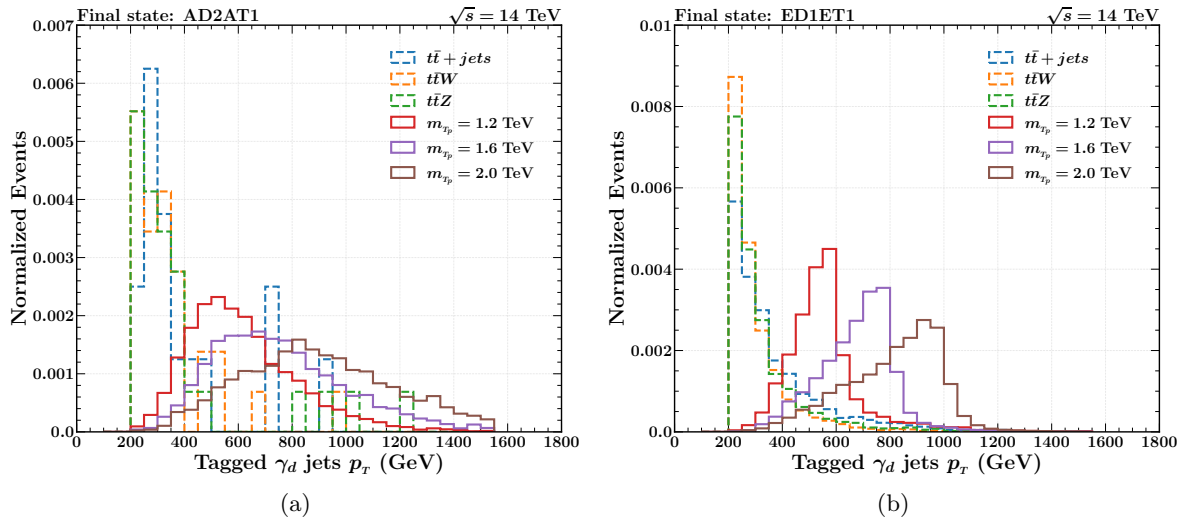


Figure 4: Same as in Fig. 3 except the LHC center of mass energy is assumed to be 14 TeV.

Invariant mass of the top-dark photon pair

We show the invariant mass distribution of the top-dark photon jet pair defined as, $M_{\gamma_d t} = \sqrt{\left| \left(p_{\gamma_d}^j + p_t^j \right)^2 \right|}$, in Fig. 5 and Fig. 6 for two different final states considered in this analysis at $\sqrt{s} = 13$ and 14 TeV, respectively.

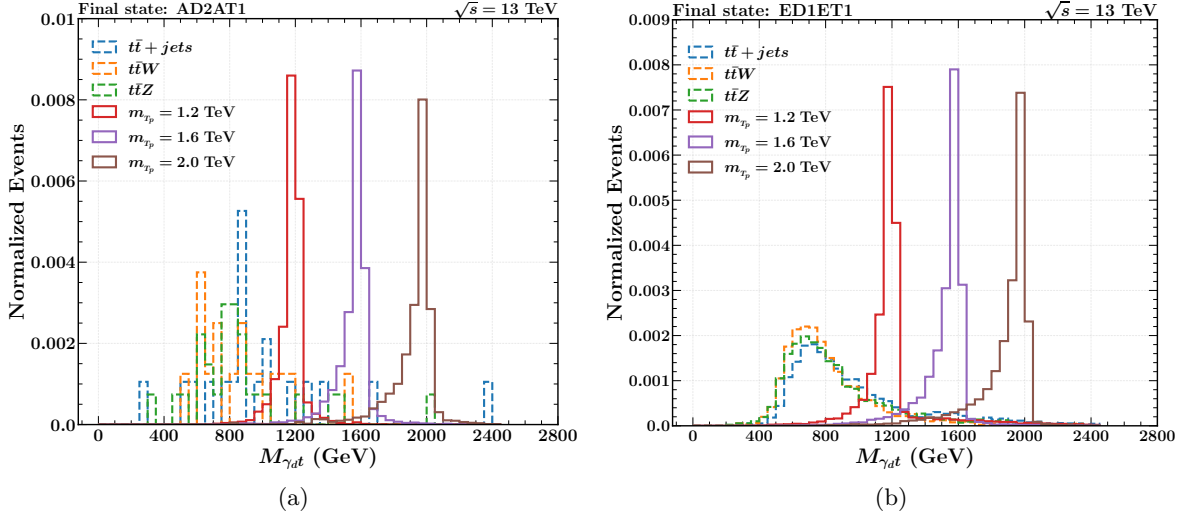


Figure 5: Invariant mass distribution of the identified dark photon and top quark system for signal and background in the (a)AD2AT1 and (b)ED1ET1 final states at 13 TeV LHC center of mass energy.

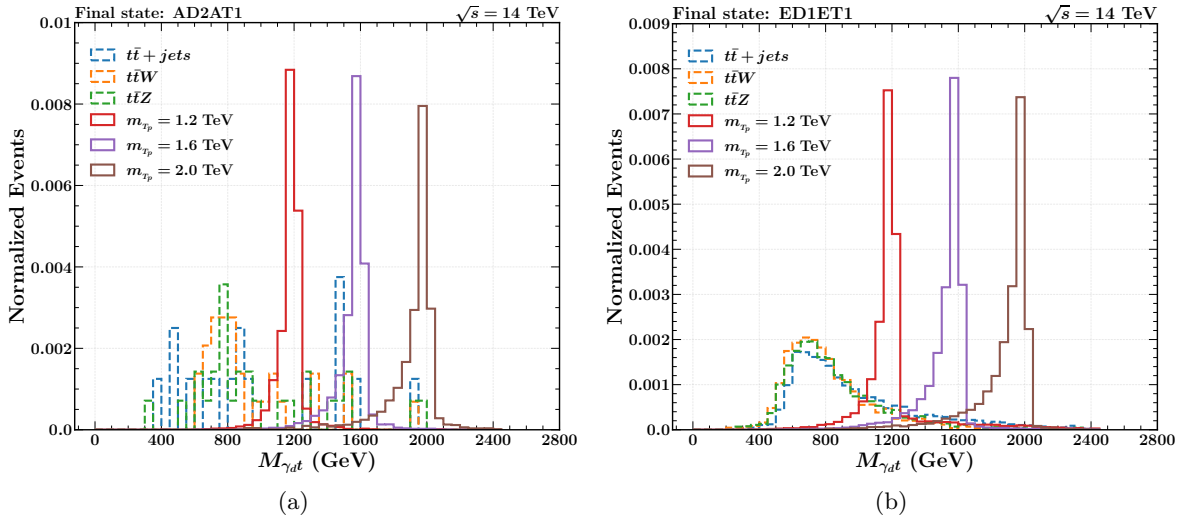


Figure 6: Same as in Fig. 5 except the LHC center of mass energy is assumed to be 14 TeV.

Based on the distributions of these kinematic variables we decide to apply a set of cuts to optimize the statistical significance of signal over the background in two different final states:

- Transverse momentum of the dark photon jet, $p_T^j > p_{T0}$.
- The invariant mass of the dark photon-top quark system to satisfy $\alpha \leq M_{\gamma_{at}} \leq \beta$.

The values of the cut parameters collectively called C_0 , are listed in Table 5 for various choices of benchmark points.

Final State	\sqrt{s} (TeV)	C_0 (GeV)	m_{T_p} (TeV)			
			1.2	1.4	1.6	1.8
AD2AT1	13 & 14	α	1100	1260	1450	1650
		β	1300	1480	1700	1900
ED1ET1	13 & 14	p_{T_0}	$0.33 \times m_{T_p}$			
		α	1100	1300	1500	1700
		β	1250	1450	1650	1850

Table 5: Values of the cut parameters (C_0) : top-dark photon invariant mass window (α , β) and minimum dark photon transverse momentum (p_{T_0}) in GeV for various choices of benchmark points in two different final states (*i.e.* AD2AT1 and ED1ET1) at $\sqrt{s} = 13$ TeV and 14 TeV in the context of LHC.

4 Results and discussions

In this section we present the results of our analysis. Table 6 and Table 7 contains the event rate for AD2AT1 and ED1ET1 final states, respectively, at both 13 TeV and 14 TeV LHC center of mass energies. In Table 6, we show the effect of cut flow in AD2AT1 final state for both signal and background. As mentioned earlier, the final state $\geq 2\gamma_d + \geq t$ which consists of *at least two dark photon and at least one top tagged jets*, has contributions from both the pair and single production of the top partner. The single production of top partner contributes when at least one or more non-dark photon jets are mistagged as dark photon jets. This final state also receives contributions from standard model background processes *e.g.*, $t\bar{t} + jets$, $t\bar{t}W$ and $t\bar{t}Z$ as already mentioned, with the dominant contribution coming from the $t\bar{t} + jets$ background. The requirement of *at least two* dark photon jets in this final state suppresses the SM background significantly due to the low mistagging rate. One can see from the Table 6 that the invariant mass of the *tagged top quark and dark photon* system can effectively suppress the standard model background in this final state.

In Table 7, we show the effect of cut flow in ED1ET1 final state for both signal and background. The final state $\gamma_d + t$ which consists of *exactly one dark photon and exactly one top tagged jets*, also receive contribution from both the pair and single production of the top partner processes. However, the relative contribution of these two processes strongly depend on the mass (m_{T_p}) and the mixing angle ($\sin\theta_L$). For example, at $\sin\theta_L = 0.1$ the single production cross-section exceeds the pair production cross-section beyond 1 TeV [5, 6]. On the other hand, for very small $\sin\theta_L$ ($\lesssim 0.02$) both the final state cross-sections will be dominated by the pair production process. The SM backgrounds for this final state are identical to those mentioned in the AD2AT1 case. The combination of the two kinematic variables, namely, (i) the transverse momentum of the tagged dark photon jet and, (ii) the invariant mass of the *tagged top quark and dark photon* system help us to optimize the signal significance in this case.

The SM background for $\gamma_d + t$ final state which is dominated by the $t\bar{t} + jets$ process is larger by a factor of 100 or more than that in the $\geq 2\gamma_d + \geq t$ final state. However, the estimated signal significance in this final state for a given benchmark point is higher than that in the $\geq 2\gamma_d + \geq t$ final state. This is due to the fact that for $\sin\theta_L = 0.1$ and $m_{T_p} \geq 1$ TeV, the single production cross-section is higher than the pair production cross-section.

The last two columns of Table 6 and 7 gives an estimate of signal significance for two different assumptions of the top partner branching ratio. The column labelled by $\text{BR}(T_p)_{100}$ assumes 100% branching ratio while $\text{BR}(T_p)_a$ represents the actual branching ratio for the top partner, respectively. The branching ratio for the dark photon decaying hadronically is assumed to be 60% throughout our analysis.

To calculate signal significance we use the following definition as obtained from the likelihood ratio method [68],

$$\sigma = \sqrt{2 \left[(s+b) \ln \left(1 + \frac{s}{b} \right) - s \right]} \quad (22)$$

Here σ quantifies the statistical significance of observing a signal s in the presence of background b . s is expected number of signal events and b is the expected number of background events. We have

assumed 139 fb^{-1} (300 fb^{-1}) of integrated luminosity at 13 (14) TeV LHC center of mass energy to obtain the signal significance.

We also consider implications of existing LHC analyses in the context of an extension of standard model with a singlet vector-like top quark partner by CMS collaboration. The CMS data corresponding to an integrated luminosity of 137 fb^{-1} at 13 TeV center of mass energy has set limits on the $\sigma(pp \rightarrow T_p b q) \times BR(T_p \rightarrow t b \bar{b})$ as a function of the top partner mass in fully hadronic final state consisting a total of seven jets, where five jets come from the decay of the top partner and three of them are b quark jets [69]. We also use the CMS limit on top partner pair production cross-section times branching ratio in the context of the same model in three different final states: single-lepton channel, same-sign dilepton channel, and “multilepton” channel with at least three leptons, corresponding to an integrated luminosity of 137 fb^{-1} at 13 TeV center of mass energy [70].

We recast these bounds in the context of the model considered in this work where the vector-like top quark acts as a portal matter and the branching ratio of the top partner in the SM mode is not necessarily fixed by the mass of the top partner (m_{T_p}) and mixing angle ($\sin \theta_L$) between the top quark and top partner. As already mentioned in sec. 2 and in [6], the top partner branching ratios both in the standard (bW , tZ , th) and in the non-standard ($t\gamma_d$, th_d) modes also depend on the vacuum expectation value of the dark higgs (v_d), mass of the dark photon (m_{γ_d}) and mass of the dark higgs (m_{h_d}). We use above CMS data to set limit in the $\sin \theta_L - m_{T_p}$ plane and corresponding exclusion limit is depicted in Fig. 7. The exclusion region in Fig. 7a corresponds to $v_d = 100 \text{ GeV}$, $m_{h_d} = 200 \text{ GeV}$, $m_{\gamma_d} = 10 \text{ GeV}$ whereas Fig. 7b corresponds to $v_d = 200 \text{ GeV}$, $m_{h_d} = 400 \text{ GeV}$, $m_{\gamma_d} = 10 \text{ GeV}$. The bounds coming from Eq. 16 and electroweak precision data are also shown by dotted and dashed line, respectively in the same plot. One can see that a large fraction of the region excluded by CMS data is already dis-favored by these constraints. We present the 2σ upper limit on the allowed values of the parameters in $\sin \theta_L - m_{T_p}$ plane in the ED1ET1 final state. As discussed above, since the ED1ET1 final state predominantly consists of events coming from the single production of the top partner, it imposes a stringent constraint on the allowed values of top and top partner mixing angle ($\sin \theta_L$). In Fig. 7 and 8, we present the 2σ exclusion limit in the $\sin \theta_L - m_{T_p}$ plane assuming *actual* $BR(T_p \rightarrow t\gamma_d)$ at $\sqrt{s} = 13$ (139 fb^{-1}) and 14 TeV (300 fb^{-1} and 3 ab^{-1}), respectively. At $\sqrt{s} = 14$ TeV with 3 ab^{-1} of integrated luminosity we have obtained a 2σ exclusion limit on $\sin \theta_L$ as low as 0.023 (0.05) upto $m_{T_p} = 1.2$ (2.0) TeV.

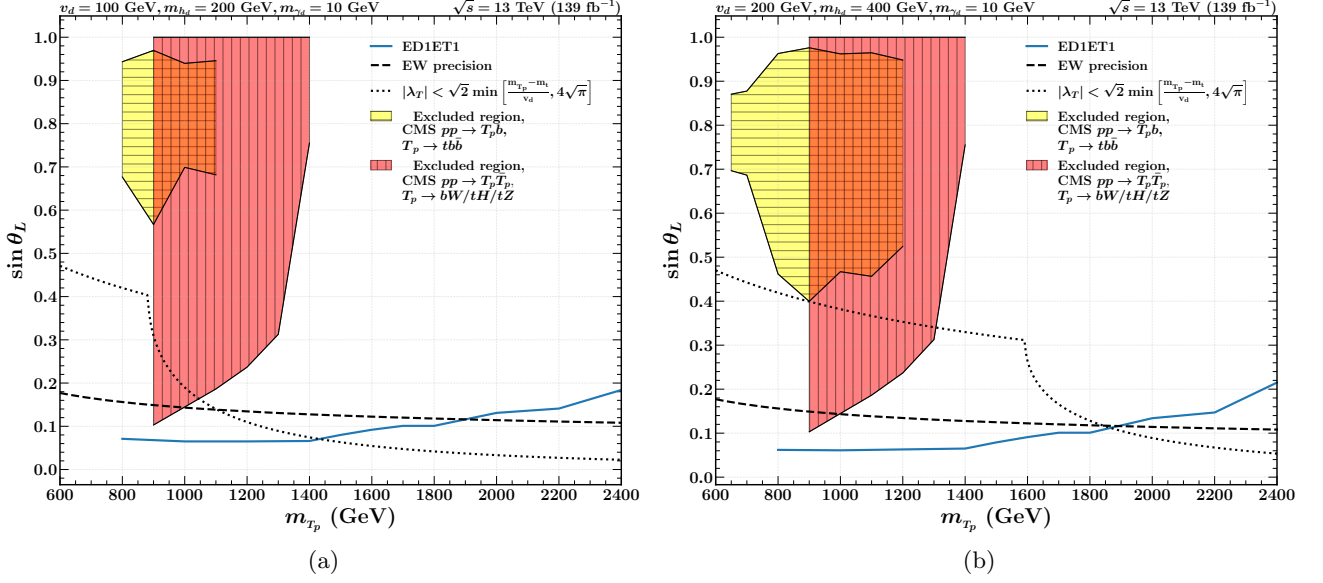


Figure 7: The exclusion limits in the $\sin \theta_L$ - m_{T_p} plane set by CMS data [69, 70] in the context of our model, as mentioned in the text, are represented by yellow (horizontal) region and red (vertical) region, respectively. The constraints coming from Eq. 16 and electroweak precision measurements are represented respectively by dotted (black) and dashed (black) lines. The solid (blue) line corresponds to the 2σ exclusion limit on the allowed values of $\sin \theta_L$ and m_{T_p} coming from our analysis in the ED1ET1 final state assuming *actual* $\text{BR}(T_p \rightarrow t\gamma_d)$ at $\sqrt{s} = 13$ TeV (139 fb^{-1}). Here, two illustrative benchmark points correspond to, (i) $v_d = 100$ GeV, $m_{h_d} = 200$ GeV, $m_{\gamma_d} = 10$ GeV and (ii) $v_d = 200$ GeV, $m_{h_d} = 400$ GeV, $m_{\gamma_d} = 10$ GeV.

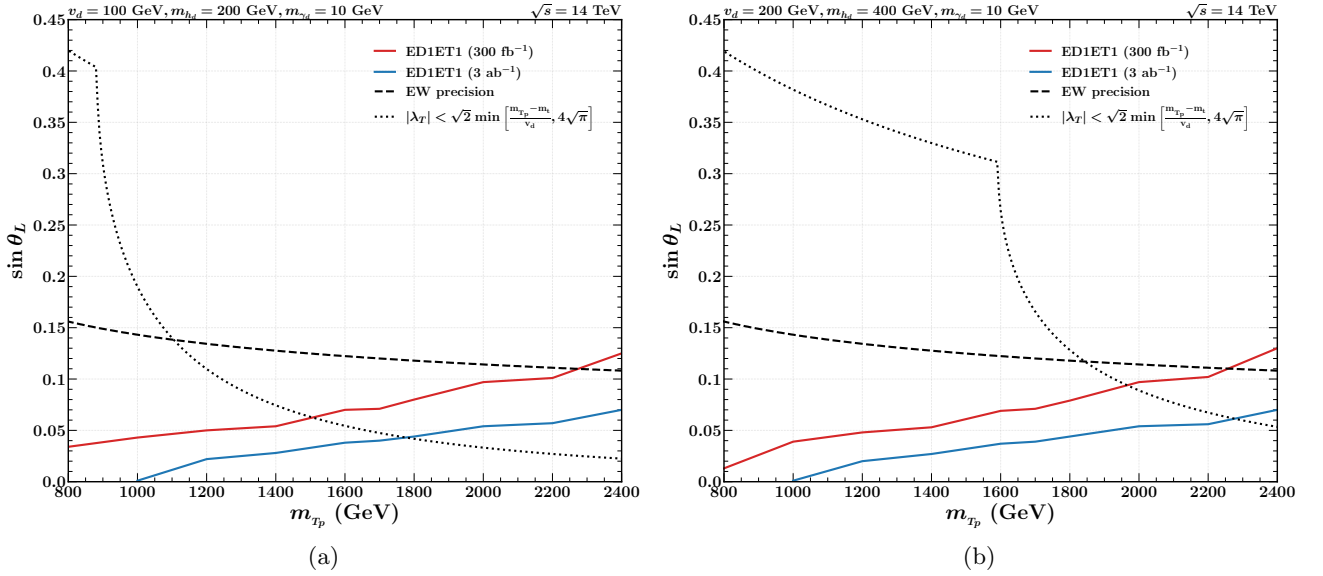


Figure 8: The exclusion limits in the $\sin \theta_L$ - m_{T_p} plane by taking into account the constraints coming from Eq. 16 and electroweak precision measurements which are represented by dotted (black) and dashed (black) lines, respectively. The red and blue (solid) lines correspond to the 2σ exclusion limit on the allowed values of $\sin \theta_L$ and m_{T_p} coming from our analysis in the the ED1ET1 final state assuming *actual* $\text{BR}(T_p \rightarrow t\gamma_d)$ at $\sqrt{s} = 14$ TeV with 300 fb^{-1} and 3 ab^{-1} integrated luminosity, respectively. Here, two illustrative benchmark points correspond to, (i) $v_d = 100$ GeV, $m_{h_d} = 200$ GeV, $m_{\gamma_d} = 10$ GeV and (ii) $v_d = 200$ GeV, $m_{h_d} = 400$ GeV, $m_{\gamma_d} = 10$ GeV.

Final state	\sqrt{s} (TeV)	m_{T_p} (TeV)	Process	Final state cross-section (fb)	$M_{\gamma_d t}$ $\in [\alpha, \beta]$ (fb)	Significance	
						$\text{BR}(T_p)_{100}$	$\text{BR}(T_p)_a$
$\geq 2\gamma_d + \geq t$ (AD2AT1)	13	1.2	Signal	0.83	0.71	10.1	3.9
			Background	0.54	0.03		
		1.4	Signal	0.36	0.31	5.4	1.9
			Background	0.54	0.03		
		1.6	Signal	0.15	0.13	2.6	0.8
			Background	0.54	0.03		
	1.8	Signal	0.06	0.04	0.8	0.2	
		Background	0.54	0.03			
	14	2.0	Signal	0.03	0.01	0.3	0.1
			Background	0.54	0.03		
		1.2	Signal	1.17	1.00	18.3	7.1
			Background	0.47	0.04		
1.4		Signal	0.53	0.46	10.0	3.5	
		Background	0.47	0.04			
1.6	Signal	0.24	0.21	4.0	1.2		
	Background	0.47	0.08				
1.8	Signal	0.10	0.08	2.4	0.7		
	Background	0.47	0.04				
2.0	Signal	0.04	0.03	1.0	0.3		
	Background	0.47	0.04				

Table 6: The effects of cut flow on cross-sections for both the signal and the total SM background in the AD2AT1 final state at $\sqrt{s} = 13$ TeV (139 fb^{-1}) and $\sqrt{s} = 14$ TeV (300 fb^{-1}). The cross-sections presented in column [5-6] assume $\text{BR}(T_p \rightarrow t\gamma_d) = 100\%$ and $\text{BR}(\gamma_d \rightarrow q\bar{q}) = 100\%$. We have assumed $\sin\theta_L = 0.1$, $v_d = 200$ GeV, $m_{\gamma_d} = 10$ GeV and $m_{h_d} = 400$ GeV to estimate the cross-sections. We present estimated signal significance in the last two columns assuming 100% and *actual* $T_p \rightarrow t\gamma_d$ BR, respectively. To estimate the signal significance we assume the hadronic branching ratio of the dark photon ($\text{BR}(\gamma_d \rightarrow q\bar{q})$) to be 60%.

Final state	\sqrt{s} (TeV)	m_{T_p} (TeV)	Process	Final state cross-section (fb)	$p_T \geq p_{T0}$ (fb)	$M_{\gamma_d t}$ $\in [\alpha, \beta]$ (fb)	Significance	
							BR(T_p) ₁₀₀	BR(T_p) _a
$\gamma_d + t$ (ED1ET1)	13	1.2	Signal	3.78	3.44	2.52	8.5	4.6
			Background	90.49	24.52	3.47		
		1.4	Signal	2.29	2.03	1.53	8.2	4.5
			Background	90.49	17.31	1.38		
		1.6	Signal	1.39	1.18	0.86	4.5	2.4
			Background	90.49	12.77	1.61		
	1.8	Signal	0.86	0.70	0.49	3.7	2.0	
		Background	90.49	9.37	0.77			
	2.0	Signal	0.53	0.42	0.28	2.2	1.2	
		Background	90.49	7.09	0.74			
	14	1.2	Signal	4.84	4.42	3.17	13.4	7.2
			Background	106.10	30.93	4.80		
1.4		Signal	2.99	2.63	1.95	12.1	6.5	
		Background	106.10	21.96	2.28			
1.6		Signal	1.84	1.56	1.14	7.8	4.1	
		Background	106.10	15.44	2.06			
1.8	Signal	1.13	0.92	0.64	5.9	3.1		
	Background	106.10	11.52	1.09				
2.0	Signal	0.75	0.59	0.39	4.1	2.1		
	Background	106.10	8.99	0.92				

Table 7: The effects of cut flow on cross-sections for both the signal and the total SM background in the ED1ET1 final state at $\sqrt{s} = 13$ TeV (139 fb^{-1}) and $\sqrt{s} = 14$ TeV (300 fb^{-1}). The cross-sections presented in column [5-7] assume $\text{BR}(T_p \rightarrow t\gamma_d) = 100\%$ and $\text{BR}(\gamma_d \rightarrow q\bar{q}) = 100\%$. We have assumed $\sin\theta_L = 0.1$, $v_d = 200$ GeV, $m_{\gamma_d} = 10$ GeV and $m_{h_d} = 400$ GeV to estimate the cross-sections. We present estimated signal significance in the last two columns assuming 100% and *actual* $T_p \rightarrow t\gamma_d$ BR, respectively. To estimate the signal significance we assume the hadronic branching ratio of the dark photon ($\text{BR}(\gamma_d \rightarrow q\bar{q})$) to be 60%.

5 Conclusions

We have considered an extension of the SM with a vector-like fermion having same quantum number as that of the right-handed top quark under the SM gauge group. In addition, the model also possesses a local $U(1)_d$ symmetry with corresponding gauge boson, *i.e.*, the dark photon. The top partner is charged under the local $U(1)_d$ gauge group while all the SM particles are neutral under it. The $U(1)_d$ symmetry is spontaneously broken by the non-zero vacuum expectation value of an additional scalar field. The top partner in this model decays to both standard ($T_p \rightarrow bW, tZ, th$) and non-standard modes ($T_p \rightarrow t\gamma_d, th_d$). The key feature of this model is that the top partner substantially decays to the non-standard modes while the branching ratio in the corresponding standard modes are suppressed in a wide range of parameter space.

The dark photon in this scenario is considered unstable and decays to a pair of SM fermions via the gauge kinetic mixing. The dark photon produced in the decay of the heavy top-partner are highly boosted, and corresponding decay products are extremely collimated. A crucial part of our analysis is to isolate a dark photon initiated jet in presence of other hadronic activity in a given event. In particular isolating it from the highly boosted top-quark and/or other jets present in the same event while also efficiently reducing the mistagging rate of non-dark photon jets present in the SM background processes. We have used a hybrid deep neural network based algorithm to identify the highly boosted dark photon initiated jet on an event-by-event basis in the dark photon mass range of 1 – 10 GeV. The method proposed in this work to identify a dark photon jet can be applied to other light exotic particles if it decays in hadronic mode and is highly boosted. However, our method is not sensitive to the spin of the light exotic particle. We have been able to achieve an average tagging efficiency of 66% to 88% for the dark photon jet in the top partner mass range, 1.2 – 1.8 TeV while the corresponding average mistagging rate for non-dark photon jets present in the signal and in the SM background varies in the range 1.0% to 1.5%.

We have considered two different final states for our analysis, namely, (i) *at least two tagged dark*

photon jet along with at least one tagged top quark jet and, (ii) exactly one tagged dark photon jet along with exactly one tagged top quark jet. We have explored the topology of the signal events, namely, the presence of highly boosted top and dark photon structure along with the fact that the invariant mass of the combined system peaks around the mass of the top partner. These immensely help us to reduce the contribution coming from the SM $t\bar{t} + jets$, $t\bar{t}W$ and, $t\bar{t}Z$ backgrounds. We have shown that with the help of certain kinematic observables such as the transverse momentum of the dark photon jet and the invariant mass of the top quark - dark photon jet system it is possible to exclude top partner mass up to 1.4 (1.7) TeV and 1.8 (2.2) TeV in the AD2AT1 and ED1ET1 final states respectively, at 13 TeV LHC center of mass energy with 139 fb^{-1} integrated luminosity assuming actual (100%) branching ratio of the top partner and $\sin \theta_L$ to be 0.1 with 2σ significance.

Additionally, we have also presented exclusion limits in the $\sin \theta_L - m_{T_p}$ plane using CMS data corresponding to 137 fb^{-1} integrated luminosity at 13 TeV LHC center of mass energy in the fully hadronic and multi-lepton (which includes single, same-sign dilepton and at least three leptons) final states in the context of single and pair production of vector-like top partner, respectively. For $\sin \theta_L > 0.3$ one can exclude m_{T_p} in the range 900 GeV - 1.3 TeV assuming $v_d = 200$ GeV. However, this limit can be relaxed if one assumes $v_d < 200$ GeV.

Finally, we have obtained the 2σ exclusion limit in $\sin \theta_L - m_{T_p}$ plane at $\sqrt{s} = 13$ TeV (139 fb^{-1}) and $\sqrt{s} = 14$ TeV (300 fb^{-1} and 3 ab^{-1}). We have shown that $\sin \theta_L$ as low as 0.023 (0.05) can be ruled out for $m_{T_p} \leq 1.2$ (2.0) TeV at 95% confidence level assuming *actual* $\text{BR}(T_p \rightarrow t\gamma_d)$ using the future LHC data corresponding to $\sqrt{s} = 14$ TeV with an integrated luminosity of 3 ab^{-1} . Our collider analysis will be applicable whenever the top partner decays to a top and dark photon and the dark photon decays promptly to a pair of SM fermions assuming m_{T_p} , $\sin \theta_L$, $\text{BR}(T_p \rightarrow t\gamma_d)$ and $\text{BR}(\gamma_d \rightarrow f\bar{f})$ as independent parameters.

Acknowledgement

We would like to thank Arun Nayak, Satyaki Bhattacharya and Shilpi Jain for useful discussion. SV is thankful for support provided by Council of Scientific & Industrial Research (CSIR, India) under CSIR-UGC NET Fellowship (File No.: 09/934(0017)/2020-EMR-I).

A Machine learning identification of dark photon jets

In this section we will detail the strategy of identifying a highly boosted dark photon jet produced in the decay of the top partner. The method described below can be applied to the dark photon produced in the decay of top partner in a wide range of its mass. Our main purpose is to identify a dark photon initiated jet in an event using hybrid deep neural network.

To identify a dark photon initiated jet in an event consisting of hadrons, we cluster the stable hadrons (including photons coming from π^0) using anti- k_T clustering algorithm with a clustering radius (R) of 0.4 to form jets. The jet momentum are reconstructed out of its constituents using p_T recombination scheme. The p_T recombination scheme is preferred over the E -scheme recombination as one gets a better reconstruction of the parton level particle momentum associated with the jet. This can be clearly seen in Fig. 9 where we compare on an event by event basis the reconstructed dark photon transverse momentum ($p_T^{\text{rec}}(\gamma_d)$) in two different schemes with true parton level dark photon transverse momentum ($p_T^{\text{true}}(\gamma_d)$).

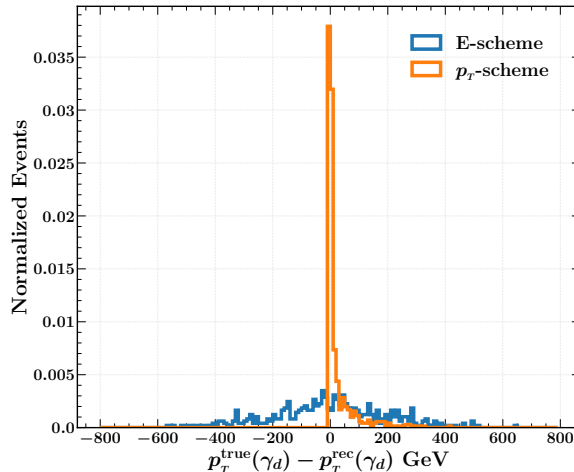


Figure 9: Comparison of reconstructed dark photon transverse momentum in the E -scheme versus p_T -scheme recombination with that of true parton level dark.

A.1 Inputs

The inputs of our hybrid deep neural network, are certain one and two-dimensional features of the potential dark photon jet candidates having $p_T > 200$ GeV. we use both the constituent level and jet level information to capture the intricate features of both, the dark photon jets and the non-dark photon jets in a binary classification framework [45–47].

The constituent level information, represented by jet images, is processed using a convolutional neural network. The CNN is adept at recognizing complex structures, such as localized p_T deposits or distinctive jet shapes. Whereas the jet-level information is processed using a Multi-Layered Perceptron. These jet level information include key features like transverse momentum of the jets, fraction of transverse momentum in a smaller cone to that of the whole jet, charge multiplicity, and charge multiplicity fraction in a smaller cone to that of the whole jet. These features offer a summary of the jet’s kinematics and characteristics of the particle content.

A.2 Jet image preprocessing

Jet image preprocessing is a crucial step to enhance the interpretability and comparability of the underlying structures within jets as well as making it easier for the HDNN model to converge faster as well as for the loss function to get closer to the global minima. To standardize the jet images in $\eta - \phi$ plane we process each jet image through three stages, namely,

1. **Centering constituents:** This process begins by centering the jet constituents along the center of the jet maintaining the range of phi in $[-\pi, \pi]$. This is achieved by transforming the η and ϕ coordinates into relative distances $\Delta\eta$ and $\Delta\phi$ from the jet’s center. This centering allows for a more consistent and clearer visualization of the decay structure within the jet.
2. **Rotating the image:** Once centered, the jet image is rotated along its principal axes to align the primary structure in a standardized orientation.
3. **Flipping the image:** The image is flipped to ensure that any additional radiations appear in the first quadrant, facilitating easier comparisons between different jets.
4. **Pixelating the image:** Finally, the image is discretized the region into a 16×16 grid with each pixel weighted by the sum of the transverse momentum in it.

This preprocessing sequence results in more uniform and comparable jet images, which are useful in helping the HDNN model to learn a standardized and coherent set of data. Moreover, the average jet images as shown in Fig. 10 give a visual representation of the preprocessed images for the dark photon and non-dark photon jets in the $\Delta\eta - \Delta\phi$ plane.

A.3 Constituent level input

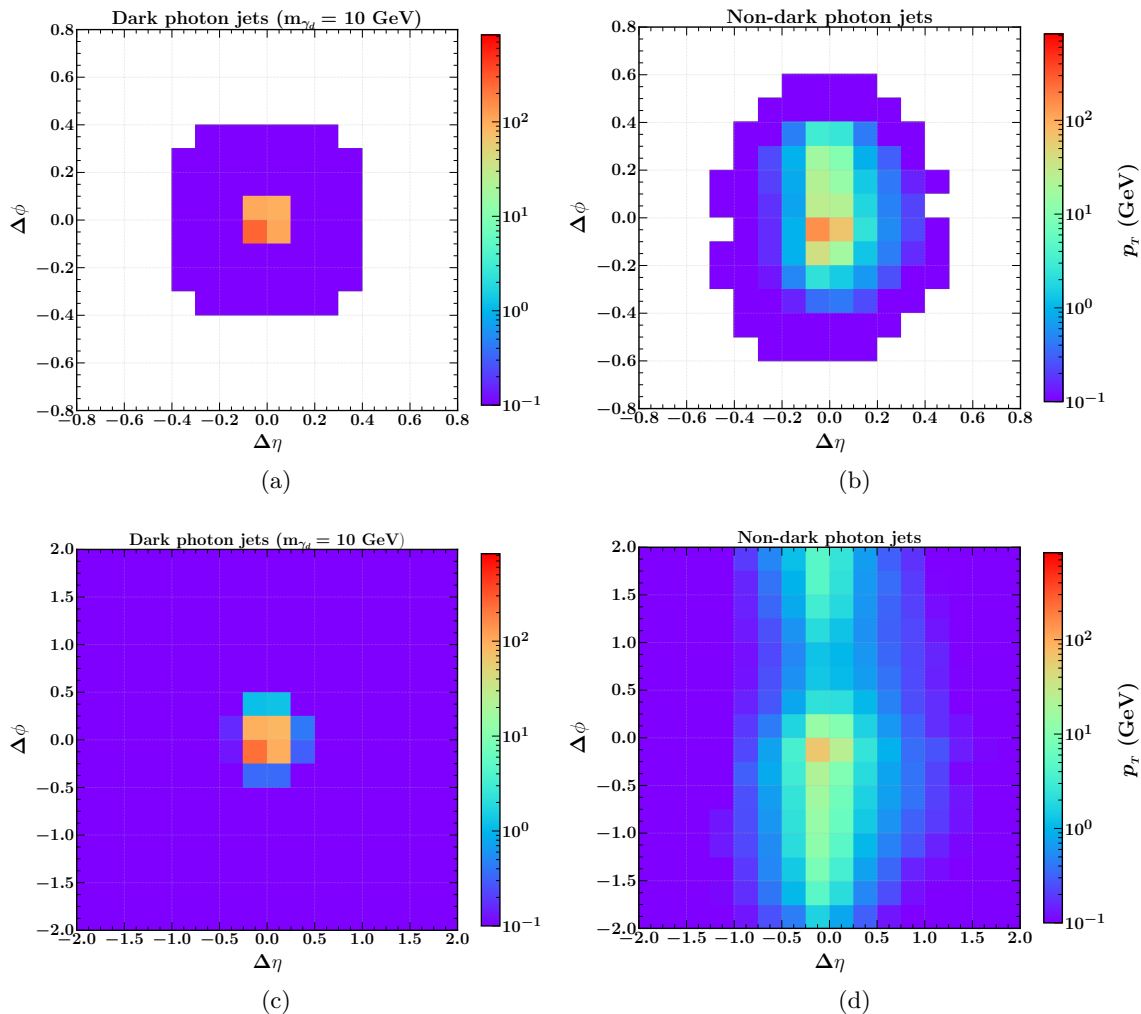


Figure 10: Average jet images for (a) dark photon jets ($m_{\gamma_d} = 10$ GeV) and (b) non-dark photon jets in the $\Delta\eta - \Delta\phi$ plane in the range -0.8 to 0.8 with granularity of 0.1×0.1 assuming $m_{T_p} = 1.4$ TeV. (c) and (d) represents the same as in (a) and (b) respectively, but in the $\Delta\eta - \Delta\phi$ range of -0.2 to 0.2 with granularity of 0.025×0.025 . Both the images above are obtained by using AK4 jets with p_T -scheme recombination.

The figures in this section display average jet images (averaged over 10,000 individual jet images) that give a visual representation of the p_T deposition of jet constituents in the $\Delta\eta - \Delta\phi$ plane for both dark photon jets and non-dark photon jets. The images are prepared with two different granularities, both having 16×16 pixels size.

In Fig. 10a and 10b we depict the jet images with a granularity of 0.1×0.1 covering a $\Delta\eta - \Delta\phi$ range from -0.8 to 0.8 for the dark photon jets and non-dark photon jets, respectively. These images include contributions from all the charged, neutral hadrons and photons, capturing the full hadronic content and providing a comprehensive representation of the jet's internal structure. Such an image captures the correlation of transverse momentum of the jet constituents with the pseudo-rapidity and azimuthal angle making it a key component in differentiating between the dark photon jets and non-dark photon jets.

On the other hand, in Fig. 10c and 10d, we present jet images with a finer granularity of 0.025×0.025 over a smaller $\Delta\eta - \Delta\phi$ range from -0.2 to 0.2 . These images include only the contributions from charged hadrons and photons. Such a finer resolution is possible if one couples the information of the ECAL energy deposition of the photons and HCAL energy deposition of the charged hadrons along with the tracker information associated with the charged hadrons. This higher resolution allows for a more detailed examination of the jet core, where most of the transverse momentum is concentrated

in the actual dark photon initiated jet. These two layers will act as two channels of the image input to the CNN part of machine learning architecture.

A.4 Jet level input

The jet level features shown in Fig. 11 play an important role in differentiating a dark photon jet from jets initiated by particles other than the dark photon. Fig. 11a shows the transverse momentum (p_T) distribution, Fig. 11b examines the p_T fraction, *i.e.* the ratio of total p_T within a cone of radius 0.2 around the jet center to that within the entire AK4 jet for the parton level tagged dark photon jet and non-dark photon jets coming from the signal (T_{pj}) itself and other SM background processes. The later variable highlights the amassing of transverse momentum for the actual dark photon jet within the jet core and is particularly significant in capturing the more highly collimated p_T depositions. Fig. 11c focuses on charge multiplicity, *i.e.*, the number of charged hadrons within the potential dark photon jet candidate. Finally, the charge multiplicity fraction, *i.e.*, the ratio of the number of charged hadrons within a cone of radius 0.2 around the jet center to that within the entire AK4 jet is shown in Fig. 11d. All these features enhance the ability to differentiate a dark photon jet from other non-dark photon jets.

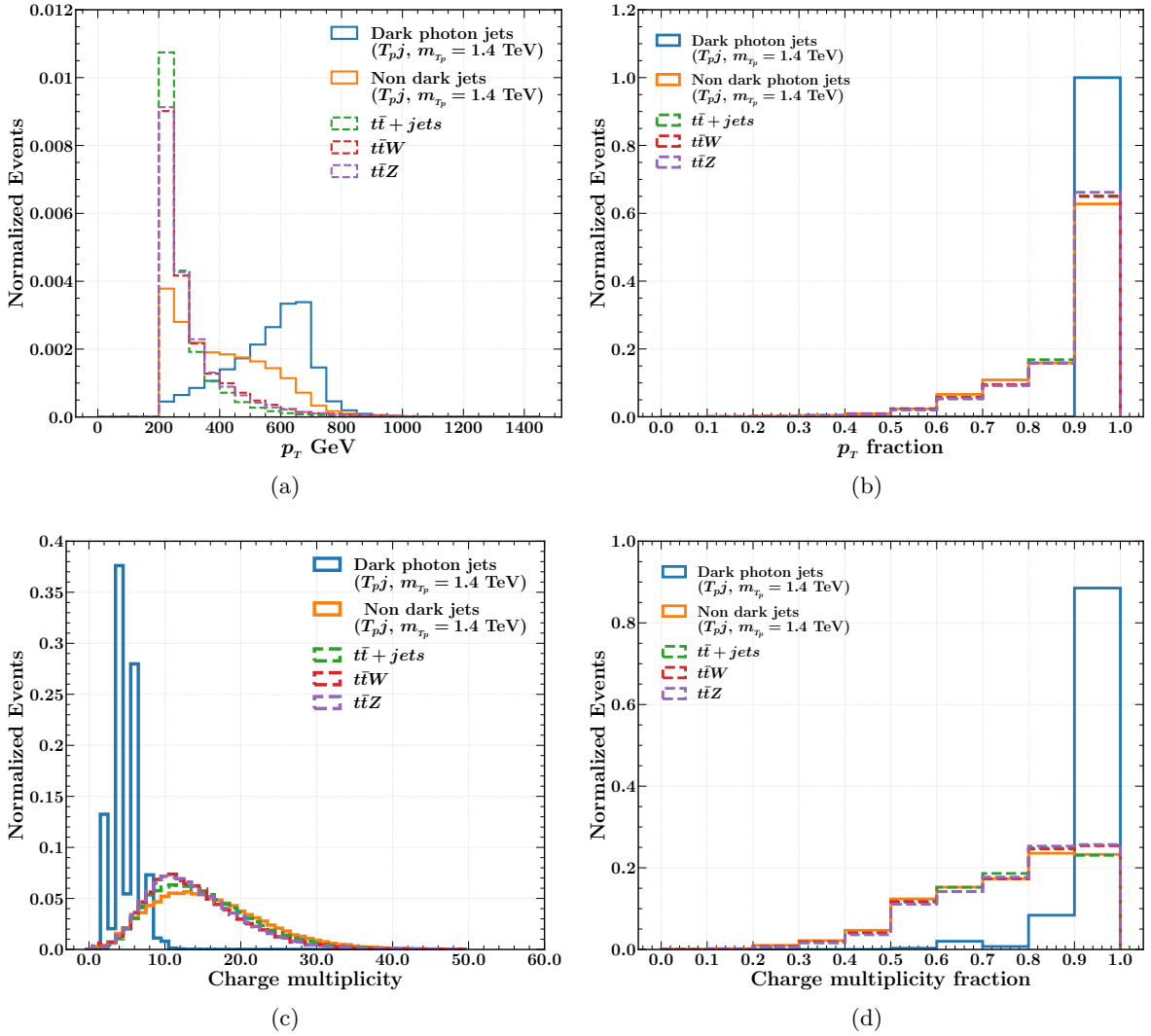


Figure 11: (a) p_T distribution, (b) ratio of total p_T within a cone of radius 0.2 around the jet center to that within the entire AK4 jet, (c) charge multiplicity distribution, and (d) ratio of the number of charged hadrons within a cone of radius 0.2 around the jet center to that within the entire AK4 jet for the parton level tagged dark photon jet and non-dark photon jets coming from the signal (T_{pj}) itself and other SM background processes.

A.5 Network architecture

The model is built to effectively process both jet images and jet-level features, making it well-suited for tasks like jet classification or tagging. The jet images are structured as $16 \times 16 \times 2$ arrays, where the individual 16×16 array represents each channel as mentioned earlier. The image input undergoes several convolutional layers, starting with a 2D convolutional layer with 32 filters and a 3×3 kernel. We also use additional padding to preserve the original image size allowing the network to preserve the spatial information throughout the layers. After this, the dimension of the array becomes $16 \times 16 \times 32$. The convolution operation is followed by a parametric rectified linear unit (PReLU) activation which introduces non-linearity, and helps the model capture complex patterns in the data. Next, another 2D convolutional layer with 64 filters is applied. The array dimension now changes $16 \times 16 \times 64$ at this stage. A third 2D convolutional layer with 64 filters is applied before the image is flattened into a 1D vector of shape 16384, converting the spatial features into a vector that can be combined with the jet-level features. Simultaneously, the jet-level features, representing kinematic variables like jet p_T , charge multiplicity, p_T and charge multiplicity fractions, are processed through a multi-layered perceptron with 64 neurons and PReLU activation. This transformation results in a latent space vector with 64 features, that complements the resultant vector resulting from flattened output from the convolutional neural network part of the HDNN. These two vectors, *i.e.*, one from the flattened jet image and the other from the jet-level features, are concatenated into a combined feature vector. At this point, the model performs dimensionality reduction through a series of fully connected layers. The first dense layer, with 64 neurons and PReLU activation. Another dense layer with 32 neurons follows, further compressing the feature vector. Finally, a dense layer with 16 neurons reduces the feature space further. The final output is generated through a sigmoid activation on a single neuron, providing a probability score between 0 and 1 for binary classification.

This model is particularly effective because it leverages both the spatial information from the jet images and the non-spatial, one dimensional jet-level features. By applying convolutional layers to the jet images, the model preserves the structure of the transverse momentum distribution across the jet, while the dense layers allow for kinematic variables of the jet.

A.6 Training and validation

The model is trained on a dataset of 240,000 samples, which is split into training and validation sets, with 80% of the data (192,000 samples) used for training and the remaining 20% (48,000 samples) used for validation. Additionally, a separate dataset of 120,000 samples is used for testing. The datasets have an equal admixture of both dark photon and non-dark photon jets, labelled as 1 and 0, respectively. During training, the model progresses through multiple epochs, each consisting of a forward and backward pass.

In each epoch, the training data is fed into the model in batches. During the forward pass, the input data is processed through various layers of the network to produce a binary output. The model's predictions are compared with the actual labels using a binary cross-entropy loss function [71], defined as:

$$\text{Loss} = -\frac{1}{N} \sum_{i=1}^N [y_i \log(p_i) + (1 - y_i) \log(1 - p_i)]$$

Where y_i represents the true label, p_i is the predicted probability for the positive class, and N is the number of samples in the batch. This loss function penalizes the model for incorrect predictions, with the penalty increasing as the prediction diverges from the true label.

We use Adam optimizer [72] to update the model's weights based on the gradients of the loss function with respect to the weights, calculated during the backward pass. The gradients are computed using backpropagation, where the error from the loss function is propagated backward through the network, updating the weights to minimize the loss. During training, the model is evaluated on the validation set at the end of each epoch to monitor its performance. We use early stopping, which halts training if the validation loss stops improving for a set number of epochs and learning rate reduction when the validation loss plateaus to prevent overfitting and improve training efficiency. After training,

the model’s performance is evaluated on a separate test dataset, providing an unbiased estimate of its generalization ability.

A.7 Model performance

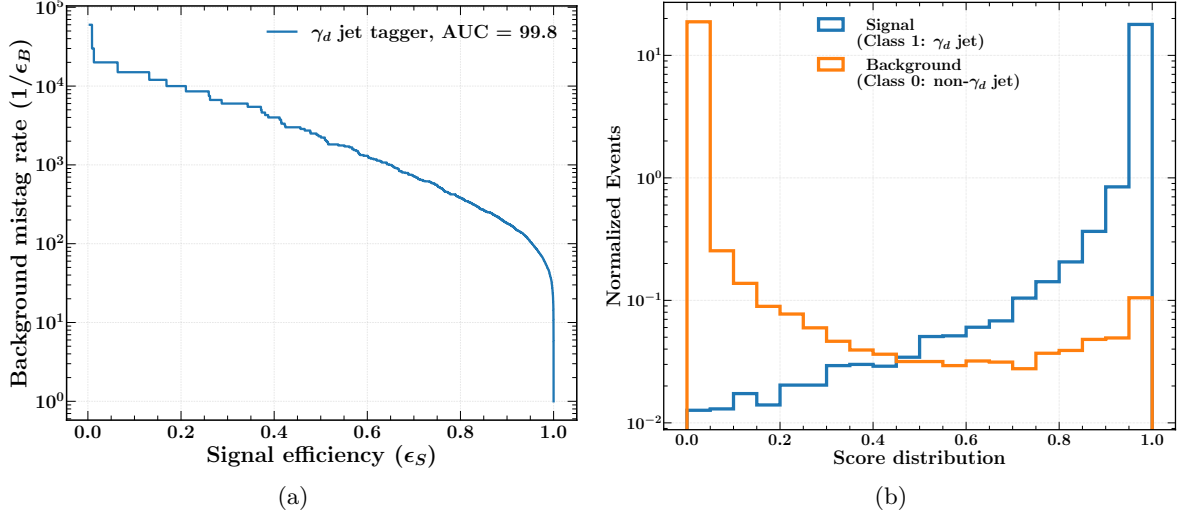


Figure 12: (a) ROC curve and (b) Score distribution for the test sample containing 60,000 parton level tagged dark photon jets and 60,000 non-dark photon jets.

Our test sample contains 60,000 parton level tagged γ_d jets and 60,000 non- γ_d jets images and corresponding jet level feature that were described in App. A.4. In Fig. 12, we illustrate the performance of our binary classification model through two key visualizations: the ROC curve and the score distribution for both signal and background events. The ROC curve in Fig. 12a provide a comprehensive view of the model’s ability to distinguish between γ_d and non- γ_d jets, with the signal efficiency plotted against the background rejection rate across different decision thresholds. A curve that approaches the top-left corner signifies a better-performing model, as it indicates high signal efficiency and strong background suppression. Additionally, the score distribution in Fig. 12b shows the clear separation achieved by the HDNN model to distinguish between a γ_d jet and a non- γ_d jet.

A.8 Efficiency

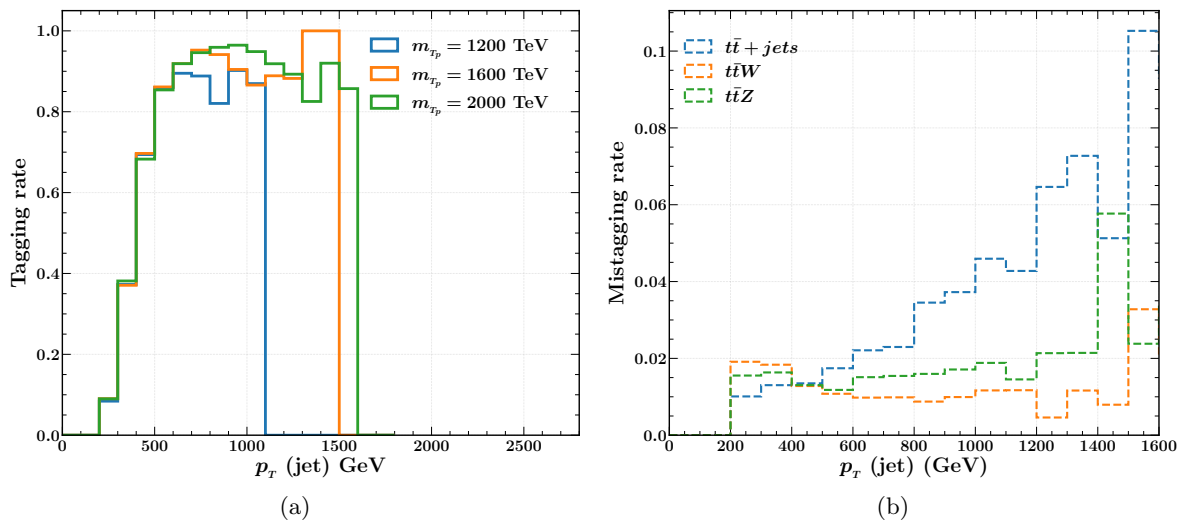


Figure 13: Tagging and mistagging rates in various transverse momentum bins for (a) parton level tagged dark photon coming from T_pj process and (b) non-dark photon jets coming various sources.

In Fig. 13, we present the tagging and mistagging rate as a function of jet p_T . We have been able to achieve an average tagging efficiency of 66% to 88% for the true dark photon jet in the top partner mass range, 1.2 – 1.8 TeV. The average mistagging rate for the corresponding non-dark photon jets present in the signal and in the SM background varies in the range 1.0% to 1.5%. For the present work it is more than sufficient to distinguish a high p_T true dark photon initiated jet having some characteristic features described above significantly different from jets initiated by other particles. In Table 8 we summarize the machine learning tagging efficiency of identifying a true dark photon jet for various choices of benchmark points relevant for present work.

	m_{T_p} (TeV)		
m_{γ_d} (GeV)	1.2	1.4	1.6
5	91%	93%	94%
10	66%	76%	82%

Table 8: Machine learning identification efficiency using the HDNN framework described above for various benchmark points assuming $m_{\gamma_d} = 10$ GeV.

References

- [1] T. G. Rizzo, *Kinetic mixing and portal matter phenomenology*, *Phys. Rev. D* **99** (Jun, 2019) 115024.
- [2] T. G. Rizzo, *Portal Matter and Dark Sector Phenomenology at Colliders*, in *2022 Snowmass Summer Study*, 2, 2022. 2202.02222.
- [3] X. Qin and J.-F. Shen, *Search for single production of vector-like B quark decaying to a Higgs boson and bottom quark at the CLIC*, *Nucl. Phys. B* **966** (2021) 115388.
- [4] G. N. Wojcik, *Kinetic Mixing from Kaluza-Klein Modes: A Simple Construction for Portal Matter*, 2205.11545.

- [5] J. H. Kim, S. D. Lane, H.-S. Lee, I. M. Lewis and M. Sullivan, *Searching for Dark Photons with Maverick Top Partners*, *Phys. Rev. D* **101** (2020) 035041, [[1904.05893](#)].
- [6] S. Verma, S. Biswas, A. Chatterjee and J. Ganguly, *Exploring maverick top partner decays at the LHC*, *Phys. Rev. D* **107** (2023) 115024, [[2209.13888](#)].
- [7] S. Gopalakrishna, T. Mandal, S. Mitra and G. Moreau, *LHC Signatures of Warped-space Vectorlike Quarks*, *JHEP* **08** (2014) 079, [[1306.2656](#)].
- [8] D. Karabacak, S. Nandi and S. K. Rai, *New signal for singlet Higgs and vector-like quarks at the LHC*, *Phys. Lett. B* **737** (2014) 341–345, [[1405.0476](#)].
- [9] J. Serra, *Beyond the Minimal Top Partner Decay*, *JHEP* **09** (2015) 176, [[1506.05110](#)].
- [10] A. Anandakrishnan, J. H. Collins, M. Farina, E. Kuflik and M. Perelstein, *Odd Top Partners at the LHC*, *Phys. Rev. D* **93** (2016) 075009, [[1506.05130](#)].
- [11] S. Banerjee, D. Barducci, G. Bélanger and C. Delaunay, *Implications of a High-Mass Diphoton Resonance for Heavy Quark Searches*, *JHEP* **11** (2016) 154, [[1606.09013](#)].
- [12] S. Kraml, U. Laa, L. Panizzi and H. Prager, *Scalar versus fermionic top partner interpretations of $t\bar{t} + E_T^{\text{miss}}$ searches at the LHC*, *JHEP* **11** (2016) 107, [[1607.02050](#)].
- [13] B. A. Dobrescu and F. Yu, *Exotic Signals of Vectorlike Quarks*, *J. Phys. G* **45** (2018) 08LT01, [[1612.01909](#)].
- [14] J. A. Aguilar-Saavedra, D. E. López-Fogliani and C. Muñoz, *Novel signatures for vector-like quarks*, *JHEP* **06** (2017) 095, [[1705.02526](#)].
- [15] M. Chala, *Direct bounds on heavy toplike quarks with standard and exotic decays*, *Phys. Rev. D* **96** (2017) 015028, [[1705.03013](#)].
- [16] S. Moretti, D. O’Brien, L. Panizzi and H. Prager, *Production of extra quarks decaying to Dark Matter beyond the Narrow Width Approximation at the LHC*, *Phys. Rev. D* **96** (2017) 035033, [[1705.07675](#)].
- [17] N. Bizot, G. Cacciapaglia and T. Flacke, *Common exotic decays of top partners*, *JHEP* **06** (2018) 065, [[1803.00021](#)].
- [18] S. Colucci, B. Fuks, F. Giacchino, L. Lopez Honorez, M. H. G. Tytgat and J. Vandecasteele, *Top-philic Vector-Like Portal to Scalar Dark Matter*, *Phys. Rev. D* **98** (2018) 035002, [[1804.05068](#)].
- [19] K. Das, T. Mondal and S. K. Rai, *Nonstandard signatures of vectorlike quarks in a leptophobic 221 model*, *Phys. Rev. D* **99** (2019) 115002, [[1807.08160](#)].
- [20] H. Han, L. Huang, T. Ma, J. Shu, T. M. P. Tait and Y. Wu, *Six Top Messages of New Physics at the LHC*, *JHEP* **10** (2019) 008, [[1812.11286](#)].
- [21] R. Dermíšek, E. Lunghi and S. Shin, *Hunting for Vectorlike Quarks*, *JHEP* **04** (2019) 019, [[1901.03709](#)].
- [22] R. Benbrik et al., *Signatures of vector-like top partners decaying into new neutral scalar or pseudoscalar bosons*, *JHEP* **05** (2020) 028, [[1907.05929](#)].
- [23] G. Cacciapaglia, T. Flacke, M. Park and M. Zhang, *Exotic decays of top partners: mind the search gap*, *Phys. Lett. B* **798** (2019) 135015, [[1908.07524](#)].
- [24] D. Wang, L. Wu and M. Zhang, *Hunting for top partner with a new signature at the LHC*, *Phys. Rev. D* **103** (2021) 115017, [[2007.09722](#)].

- [25] S. Dasgupta, R. Pramanick and T. S. Ray, *Broad topline vector quarks at LHC and HL-LHC*, *Phys. Rev. D* **105** (2022) 035032, [2112.03742].
- [26] A. Bhardwaj, T. Mandal, S. Mitra and C. Neeraj, *Roadmap to explore vectorlike quarks decaying to a new scalar or pseudoscalar*, *Phys. Rev. D* **106** (2022) 095014, [2203.13753].
- [27] A. Bhardwaj, K. Bhide, T. Mandal, S. Mitra and C. Neeraj, *Discovery prospects of a vectorlike top partner decaying to a singlet boson*, *Phys. Rev. D* **106** (2022) 075024, [2204.09005].
- [28] J. Bardhan, T. Mandal, S. Mitra and C. Neeraj, *Machine learning-enhanced search for a vectorlike singlet B quark decaying to a singlet scalar or pseudoscalar*, *Phys. Rev. D* **107** (2023) 115001, [2212.02442].
- [29] J. a. M. Alves, G. C. Branco, A. L. Cherchiglia, C. C. Nishi, J. T. Penedo, P. M. F. Pereira et al., *Vector-like singlet quarks: A roadmap*, *Phys. Rept.* **1057** (2024) 1–69, [2304.10561].
- [30] A. Banerjee, V. Ellajosyula and L. Panizzi, *Heavy vector-like quarks decaying to exotic scalars: a case study with triplets*, *JHEP* **01** (2024) 187, [2311.17877].
- [31] A. Banerjee, E. Bergeaas Kuutmann, V. Ellajosyula, R. Enberg, G. Ferretti and L. Panizzi, *Vector-like quarks: status and new directions at the LHC*, 2406.09193.
- [32] G. Corcella, A. Costantini, M. Ghezzi, L. Panizzi, G. M. Pruna and J. Šalko, *Vector-like quarks decaying into singly and doubly charged bosons at LHC*, *JHEP* **10** (2021) 108, [2107.07426].
- [33] R. Dermisek, E. Lunghi, N. McGinnis and S. Shin, *Tau-jet signatures of vectorlike quark decays to heavy charged and neutral Higgs bosons*, *JHEP* **08** (2021) 159, [2105.10790].
- [34] K. du Plessis, M. M. Flores, D. Kar, S. Sinha and H. van der Schyf, *Hitting two BSM particles with one lepton-jet: search for a top partner decaying to a dark photon, resulting in a lepton-jet*, *SciPost Phys.* **13** (2022) 018, [2112.08425].
- [35] M. Fabbrichesi, E. Gabrielli and G. Lanfranchi, *The Dark Photon*, 2005.01515.
- [36] M. Bauer, P. Foldenauer and J. Jaeckel, *Hunting All the Hidden Photons*, *JHEP* **07** (2018) 094, [1803.05466].
- [37] L. de Oliveira, M. Kagan, L. Mackey, B. Nachman and A. Schwartzman, *Jet-images — deep learning edition*, *JHEP* **07** (2016) 069, [1511.05190].
- [38] G. Kasieczka, T. Plehn, M. Russell and T. Schell, *Deep-learning Top Taggers or The End of QCD?*, *JHEP* **05** (2017) 006, [1701.08784].
- [39] ATLAS collaboration, *Quark versus Gluon Jet Tagging Using Jet Images with the ATLAS Detector*, tech. rep., CERN, Geneva, 2017.
- [40] A. J. Larkoski, I. Moult and B. Nachman, *Jet Substructure at the Large Hadron Collider: A Review of Recent Advances in Theory and Machine Learning*, *Phys. Rept.* **841** (2020) 1–63, [1709.04464].
- [41] K. Albertsson et al., *Machine Learning in High Energy Physics Community White Paper*, *J. Phys. Conf. Ser.* **1085** (2018) 022008, [1807.02876].
- [42] Y.-L. Chung, S.-C. Hsu and B. Nachman, *Disentangling Boosted Higgs Boson Production Modes with Machine Learning*, *JINST* **16** (2021) P07002, [2009.05930].
- [43] M. Andrews et al., *End-to-end jet classification of boosted top quarks with the CMS open data*, *EPJ Web Conf.* **251** (2021) 04030, [2104.14659].
- [44] J. Kim et al., *Large-Scale Deep Learning for Multi-Jet Event Classification*, 2207.11710.

- [45] CMS collaboration, A. Tumasyan et al., *Identification of hadronic tau lepton decays using a deep neural network*, *JINST* **17** (2022) P07023, [[2201.08458](#)].
- [46] A. Hammad, S. Khalil and S. Moretti, *Search for mono-Higgs signals in bb^- final states using deep neural networks*, *Phys. Rev. D* **107** (2023) 075027, [[2208.10133](#)].
- [47] K. Ban, K. Kong, M. Park and S. C. Park, *Exploring the Synergy of Kinematics and Dynamics for Collider Physics*, [2311.16674](#).
- [48] T. Robens and T. Stefaniak, *Status of the Higgs Singlet Extension of the Standard Model after LHC Run 1*, *Eur. Phys. J. C* **75** (2015) 104, [[1501.02234](#)].
- [49] T. Robens, *Investigating extended scalar sectors at current and future colliders*, *PoS LHCP2019* (2019) 138, [[1908.10809](#)].
- [50] T. Robens, *More Doublets and Singlets*, in *56th Rencontres de Moriond on Electroweak Interactions and Unified Theories*, 5, 2022. [2205.06295](#).
- [51] S. Adhikari, S. D. Lane, I. M. Lewis and M. Sullivan, *Complex Scalar Singlet Model Benchmarks for Snowmass*, in *Snowmass 2021*, 3, 2022. [2203.07455](#).
- [52] S. D. Lane, I. M. Lewis and M. Sullivan, *Resonant multiscalar production in the generic complex singlet model in the multi-TeV region*, *Phys. Rev. D* **110** (2024) 055017, [[2403.18003](#)].
- [53] T. Robens, *Constraining extended scalar sectors at current and future colliders - an update*, in *8th Workshop on Theory, Phenomenology and Experiments in Flavour Physics: Neutrinos, Flavor Physics and Beyond*, 9, 2022. [2209.15544](#).
- [54] CMS collaboration, A. Tumasyan et al., *A search for decays of the Higgs boson to invisible particles in events with a top-antitop quark pair or a vector boson in proton-proton collisions at $\sqrt{s} = 13$ TeV*, *Eur. Phys. J. C* **83** (2023) 933, [[2303.01214](#)].
- [55] ATLAS collaboration, G. Aad et al., *Combination of searches for invisible decays of the Higgs boson using 139 fb^{-1} of proton-proton collision data at $s=13$ TeV collected with the ATLAS experiment*, *Phys. Lett. B* **842** (2023) 137963, [[2301.10731](#)].
- [56] M. Buchkremer, G. Cacciapaglia, A. Deandrea and L. Panizzi, *Model Independent Framework for Searches of Top Partners*, *Nucl. Phys. B* **876** (2013) 376–417, [[1305.4172](#)].
- [57] J. H. Kim and I. M. Lewis, *Loop Induced Single Top Partner Production and Decay at the LHC*, *JHEP* **05** (2018) 095, [[1803.06351](#)].
- [58] PARTICLE DATA GROUP collaboration, P. A. Zyla et al., *Review of Particle Physics*, *PTEP* **2020** (2020) 083C01.
- [59] J. Alwall, R. Frederix, S. Frixione, V. Hirschi, F. Maltoni, O. Mattelaer et al., *The automated computation of tree-level and next-to-leading order differential cross sections, and their matching to parton shower simulations*, *JHEP* **07** (2014) 079, [[1405.0301](#)].
- [60] A. Alloul, N. D. Christensen, C. Degrande, C. Duhr and B. Fuks, *FeynRules 2.0 - A complete toolbox for tree-level phenomenology*, *Comput. Phys. Commun.* **185** (2014) 2250–2300, [[1310.1921](#)].
- [61] C. Degrande, C. Duhr, B. Fuks, D. Grellscheid, O. Mattelaer and T. Reiter, *UFO - The Universal FeynRules Output*, *Comput. Phys. Commun.* **183** (2012) 1201–1214, [[1108.2040](#)].
- [62] R. D. Ball et al., *Parton distributions with LHC data*, *Nucl. Phys. B* **867** (2013) 244–289, [[1207.1303](#)].
- [63] C. Bierlich et al., *A comprehensive guide to the physics and usage of PYTHIA 8.3*, [2203.11601](#).

- [64] D. E. Kaplan, K. Rehermann, M. D. Schwartz and B. Tweedie, *Top Tagging: A Method for Identifying Boosted Hadronically Decaying Top Quarks*, *Phys. Rev. Lett.* **101** (2008) 142001, [[0806.0848](#)].
- [65] M. Cacciari, G. P. Salam and G. Soyez, *FastJet User Manual*, *Eur. Phys. J. C* **72** (2012) 1896, [[1111.6097](#)].
- [66] S. Bentvelsen and I. Meyer, *The Cambridge jet algorithm: Features and applications*, *Eur. Phys. J. C* **4** (1998) 623–629, [[hep-ph/9803322](#)].
- [67] M. L. Mangano, M. Moretti and R. Pittau, *Multijet matrix elements and shower evolution in hadronic collisions: $Wb\bar{b} + n$ jets as a case study*, *Nucl. Phys. B* **632** (2002) 343–362, [[hep-ph/0108069](#)].
- [68] G. Cowan, K. Cranmer, E. Gross and O. Vitells, *Asymptotic formulae for likelihood-based tests of new physics*, *Eur. Phys. J. C* **71** (2011) 1554, [[1007.1727](#)].
- [69] CMS collaboration, A. Hayrapetyan et al., *Search for production of a single vector-like quark decaying to th or tz in the all-hadronic final state in pp collisions at $\sqrt{s} = 13$ tev*, [2405.05071](#).
- [70] CMS collaboration, A. Tumasyan et al., *Search for pair production of vector-like quarks in leptonic final states in proton-proton collisions at $\sqrt{s} = 13$ tev*, *JHEP* **07** (2023) 020, [[2209.07327](#)].
- [71] A. Mao, M. Mohri and Y. Zhong, *Cross-entropy loss functions: Theoretical analysis and applications*, *ArXiv* [abs/2304.07288](#) (2023) .
- [72] D. P. Kingma and J. Ba, *Adam: A method for stochastic optimization*, 2017.